An above-ground biomass map of African savannahs and woodlands at 25 m resolution derived from ALOS PALSAR

Alexandre Bouvet, Stéphane Mermoz, Thuy Le Toan, Ludovic Villard, Renaud Mathieu, Laven Naidoo, Gregory P Asner

Remote Sensing of Environment 206 (2018) 156–173

Contents lists available at ScienceDirect

Remote Sensing of Environment

journal homepage: www.elsevier.com/locate/rse

An above-ground biomass map of African savannahs and woodlands at 25 m resolution derived from ALOS PALSAR

Alexandre Bouvet[a,*], Stéphane Mermoz[a], Thuy Le Toan[a], Ludovic Villard[a], Renaud Mathieu[b], Laven Naidoo[b], Gregory P. Asner[c]

[a] CESBIO, Université de Toulouse, CNES/CNRS/IRD/UPS, Toulouse, France
[b] Ecosystems Earth Observation, Natural Resource and the Environment, CSIR, Pretoria, South Africa
[c] Department of Global Ecology, Carnegie Institution for Science, Stanford, CA, USA

ARTICLE INFO

Keywords:
Above-ground biomass
Africa
PALSAR
Savannahs
Woodlands

ABSTRACT

Savannahs and woodlands are among the most important biomes in Africa: they cover half of sub-Saharan Africa, provide vital ecosystem services to the rural communities, and play a major part in the carbon budget. Despite their importance and their fragility, they are much less studied than other ecosystems like rainforests. In particular, the distribution and amount of the above-ground woody biomass (AGB) is largely unknown. In this paper, we produce the first continental map of the AGB of African savannahs and woodlands at a resolution of 25 m. The map is built from the 2010 L-band PALSAR mosaic produced by JAXA, along the following steps: a) stratification into wet/dry season areas in order to account for seasonal effects, b) development of a direct model relating the PALSAR backscatter to AGB, with the help of *in situ* and ancillary data, c) Bayesian inversion of the direct model. A value of AGB and its uncertainty has been assigned to each pixel. This approach allows estimating AGB until 85 $Mg{\cdot}ha^{-1}$ approximately, while dense forests and non-vegetated areas are masked out using the ESA CCI Land Cover dataset. The resulting map is visually compared with existing AGB maps and is validated using a cross-validation approach and a comparison with AGB estimates obtained from LiDAR datasets, leading to an RMSD of 8 to 17 $Mg{\cdot}ha^{-1}$. Finally, carbon stocks for savannahs in Africa and in 50 countries are estimated and compared with estimates by FAO and from AGB maps available over Africa.

1. Introduction

The role of the African continent in the global carbon cycle has received increasing attention over the last decade (Bombelli et al., 2009; Ciais et al., 2009, 2011; Houghton and Hackler, 2006; Valentini et al., 2014; Williams et al., 2007). Although large uncertainties affect the continental estimation of the carbon budget, most recent studies agree that Africa is currently a small sink of carbon, with an average value of -0.61 ± 0.58 $Pg{\cdot}C{\cdot}yr^{-1}$ (Valentini et al., 2014). Africa is also a major source of interannual variability in the global atmospheric CO_2 concentration (Williams et al., 2007). The uncertainties and interannual variations associated to these estimates mostly involve savannahs and woodlands, whose contribution to the carbon budget is much more important in Africa than in the other tropical regions such as South America or Southeast Asia. Indeed, while the carbon density of savannahs and woodlands is lower than that of closed forests, they cover three times larger areas in Africa (Bartholomé and Belward, 2005), *e.g.* roughly 50% of the continent, and therefore represent a large carbon stock. Besides, with low – although increasing – fossil fuel emissions, the carbon balance of Africa is currently dominated by the uptake and release from terrestrial ecosystems, which is controlled by climate fluctuations and human-induced disturbances, both of which have stronger effects in savannahs and woodlands than in other ecosystems in Africa. For example fires, which play a significant role in the African carbon cycle with 1.03 ± 0.22 $Pg{\cdot}C{\cdot}yr^{-1}$ of carbon emissions, occur in savannahs and dry woodlands in 90% of the cases (Valentini et al., 2014). Deforestation rates in African savannah woodlands are found to be higher than in tropical rain forests, where massive deforestation has been avoided so far, in favour of selective logging (Brink and Eva, 2009; Ciais et al., 2011). Woody encroachment also appears to be a widespread source of change in the carbon stocks of these biomes (Mitchard and Flintrop, 2013). It is therefore important to accurately estimate and monitor the carbon stocks of African savannahs and woodlands in order to have a better knowledge of the African and global carbon budget.

Until recently, our knowledge of the global distribution and amount of woody carbon stocks was mostly based on field measurements of

* Corresponding author.
E-mail addresses: alexandre.bouvet@cesbio.cnes.fr (A. Bouvet), stephane.mermoz@cesbio.cnes.fr (S. Mermoz), thuy.letoan@cesbio.cnes.fr (T. Le Toan), ludovic.villard@cesbio.cnes.fr (L. Villard), rmathieu@csir.co.za (R. Mathieu), lnaidoo@csir.co.za (L. Naidoo), gpa@carnegiescience.edu (G.P. Asner).

https://doi.org/10.1016/j.rse.2017.12.030
Received 9 December 2016; Received in revised form 24 November 2017; Accepted 18 December 2017

relatively small-size plots, which fail to adequately account for the spatial variability of their surrounding areas (Réjou-Méchain et al., 2014), and which are not uniformly distributed over the different forested biomes (Gibbs and Brown, 2007; Houghton et al., 2009). For instance, forest plantations are fairly well represented through commercial inventories but savannahs and woodlands, with no commercial value, have received much less attention. Also, they are not always considered as forests regarding the United Nations Framework Convention on Climate Change national forest definitions, and may therefore be disregarded in some monitoring activities. Besides, most carbon estimates are based on a handful of biome-average datasets where a single representative value of forest carbon per unit area is applied to broad forest categories or biomes (Achard et al., 2002, 2004; DeFries et al., 2002; Fearnside, 2000; Houghton et al., 2009; Ramankutty et al., 2007). Such approaches have led to large inconsistencies between studies. In the past few years, remote sensing approaches have offered considerable potential in support of woody carbon mapping as they provide long-term and repetitive observations over large areas. However, optical data, such as provided by the MODerate resolution Imaging Spectroradiometer (MODIS) or Landsat, are not sensitive to woody above ground biomass (AGB) beyond the canopy closure, and for savannahs and woodlands, are contaminated by the grass layer present in these open landscapes (Naidoo et al., 2016; Zeidler et al., 2012). Spaceborne LiDAR data (*e.g.* ICESat GLAS) are less suitable for open savannahs and woodlands and are limited by discontinuous coverage (Lefsky et al., 2005). Combinations of ICESat GLAS data with MODIS data have been developed to produce large-scale pan-tropical AGB maps. The approach consists in spatially extrapolating above ground woody carbon stocks obtained from *in situ* inventory plots and from ICESat GLAS transects, using MODIS only (Baccini et al., 2012) or using MODIS and Quick Scatterometer (QuikSCAT) data (Saatchi et al., 2011). While these two pan-tropical biomass maps, being the first of their kind with such a large coverage, have been widely used, they however suffer from a number of limitations: they have low spatial resolutions (0.5 to 1 km), no temporal repetition, and show large uncertainties (Mitchard et al., 2013a). In order to reduce the biases and improve the accuracy, independent reference plot datasets have been used to combine these two maps into an integrated map (Avitabile et al., 2016), but the limitations related to spatial and temporal resolutions remain. An update of the Baccini map has been recently produced at 30 m resolution, using Landsat data, and is available in the Global Forest Watch project (Baccini et al., 2015), but with reported large uncertainty at pixel level. For savannahs and woodlands in Africa, the uncertainty is expected to be very large, because of the above mentioned limitations of MODIS, Landsat, and ICEsat, worsened by the sparser GLAS coverage of such ecosystems used in the production of these datasets.

It has long been known that SAR data have high potential for AGB mapping and AGB stocks estimation, due to the relationships between the SAR backscatter and biomass (Le Toan et al., 1992). These relationships are affected by other parameters such as soil moisture (Harrell et al., 1997; Kasischke et al., 2011), topography (Castel et al., 2001), or the forest structure (Imhoff, 1995), which requires the adoption of specific strategies to mitigate the impacts of these environmental effects on the retrieval of AGB. Despite these limitations, SAR systems remain a promising tool for AGB estimation. Generally speaking, the backscatter in images acquired at short wavelengths like X-band or C-band show little dependence on biomass, although it has been shown that this weak sensitivity can be counterbalanced with the use of hyper-temporal observations, in particular in boreal forests (Santoro et al., 2011, 2013). Images acquired at long wavelengths like L-band or P-band are more strongly correlated with AGB. In the last decades, L-band spaceborne SAR data have become available, with the JERS-1 satellite active from 1992 to 1999 and ALOS PALSAR from 2006 to 2011, followed by PALSAR-2 onboard ALOS-2 launched in May 2014. SAOCOM (SAtélite Argentino de Observación COn Microondas) and NISAR (NASA/ISRO SAR Mission) L-band SAR systems are planned for launch in 2018 and 2020 respectively. Many theoretical and experimental studies showed that L-band SAR data are sensitive to forest AGB until a saturation level is reached and sensitivity is lost; however, a negative correlation between L-band backscatter and high AGB may occur when the forest is dense (Mermoz et al., 2015). The saturation is generally reported to occur between 70 and 150 $Mg{\cdot}ha^{-1}$ (Mermoz et al., 2014; Mitchard et al., 2009; Yu and Saatchi, 2016), depending on the experimental dataset and on the model used to relate the backscatter to AGB. L-band SAR data are therefore well suited to the estimation of savannah AGB, typically below 100 $Mg{\cdot}ha^{-1}$. For the denser woodlands, typically between 100 and 200 $Mg{\cdot}ha^{-1}$, and higher biomass values, P-band SAR systems have a better potential, but are not available so far in space because of frequency allocation limitations that were lifted only recently. The BIOMASS mission (Le Toan et al., 2011), planned for launch by the European Space Agency in 2021, will fill this gap and make it possible to exploit the synergy between L-band and P-band. Yearly PALSAR (2007–2010) and PALSAR-2 (2015-onwards) mosaics at 25 m have been built by the Japan Aerospace Exploration Agency (JAXA), and are freely available (http://www.eorc.jaxa.jp/ALOS/en/palsar_fnf/fnf_index.htm), which facilitates the use of large datasets for forest monitoring (Shimada et al., 2014). In the recent years, ALOS PALSAR data have therefore been used for AGB estimation in savannahs and woodlands for limited regions or countries in Africa and Australia (Carreiras et al., 2012, 2013; Lucas et al., 2010; Mermoz et al., 2014; Mitchard et al., 2009, 2011; Mitchard et al., 2013b; Naidoo et al., 2015; Ribeiro et al., 2008). However, these local studies have not been extended so far to continental scales, therefore the amount and distribution of the AGB in the whole African savannahs and woodlands remains to be better quantified (Bastin et al., 2017).

In this paper, we aim at filling this gap, by estimating woody AGB at a spatial resolution of 25 m over the entire savannah biome of Africa using ALOS PALSAR 2010 mosaics. The method comprises two steps. The first step consists in defining a direct model that relates the PALSAR backscatter to AGB, with the help of a selected set of field measurements. In the second step, a Bayesian inversion of this model is performed to produce the AGB gridded dataset. The paper is organised as follows: Section 2 gives general information on the savannahs of the African continent. Section 3 provides information on the data used in this study, both *in situ* plot data and SAR data. Section 4 presents the data analysis results and describes the development of the direct model as well as the Bayesian inversion scheme. Section 5 discusses the resulting estimates of savannah woody biomass in Africa and their associated uncertainties, and provides a validation assessment and a comparison with other large-scale AGB datasets available over Africa and national statistics.

2. Study area

2.1. Demography, climate and biomes

The African continent covers more than $30Mkm^2$, which accounts for 20% of the Earth's land surface. The estimated population is nearly 1.2 billion people, mostly concentrated in savannah and woodland landscapes (Chidumayo and Gumbo, 2010), and increases nearly three times faster than in the rest of the world; demographers now project that Africa's inhabitants will triple or quadruple by the end of this century (Engelman, 2016). Africa comprises 54 member states of the United Nations, among which 28 are partner countries supported by the UN-REDD programme.

Africa lies mainly within the inter-tropical zone and is therefore a consistently hot continent. The different climate zones are therefore characterized primarily by their rainfall regimes. The number of dry months per year is shown in Fig. 1. It was produced using the mean monthly precipitations measured by the Tropical Rainfall Measuring Mission (TRMM) between 1998 and 2016 (3B43 products at a

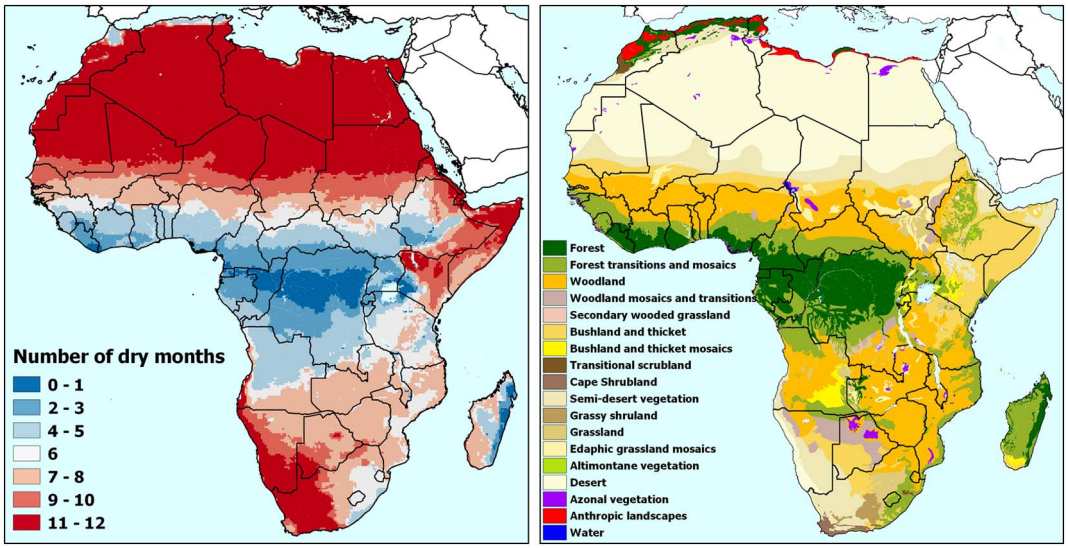

Fig. 1. (Left) Map of the number of dry months per year in Africa, and (Right) the UNESCO vegetation map of Africa.

0.25° × 0.25° resolution accessed through the Earthdata portal https://earthdata.nasa.gov/), where a 60 mm monthly rainfall threshold has been applied to define dry months following the threshold applied for tropical climates in the Köppen climate classification (Köppen, 1936). The rainfall regime controls the dominant vegetation types, which is depicted in Fig. 1 following the UNESCO vegetation map of Africa (White, 1984). The equatorial climate zone, characterized by high rainfalls throughout the year, with no dry season, is the home of evergreen rain forests, which are found in Africa mostly over the Congo Basin - the second largest tropical rainforest in the world - as well as in Western Africa and Madagascar. In regions with a short dry season (2 to 3 dry months per year), the evergreen rain forests transition to more open landscapes, and as the length of the dry season increases, the proportion of trees in the landscape decreases, from woodlands (approximately 4 to 8 dry months per year) to bushlands and grasslands (9 to 10 dry months per year). Obviously, in the most arid regions (11–12 dry months per year), a desert or semi-desert landscape prevails.

In this paper, we focus on the low woody biomass areas, which therefore exclude dense forests and deserts. For simplicity, in this paper such areas will be referred to as “savannahs”, understood in its broadest sense, *i.e.* a subtropical or tropical grassland region with scattered trees, grading from open plain to woodland. The term “savannahs” therefore represents any kind of mixed tree-grass ecosystems, including woodlands and most dry forests, which stay below the canopy closure. Referred to Fig. 1, the regions under study encompass most classes from the UNESCO vegetation map except the forest and the desert classes, which represents roughly 50% of the continent area.

As a physiological response to the water shortage during the dry season, most tree species from these areas have a deciduous foliage and lose their leaves at some point in the dry months. However, within a region, the leaf fall and leaf emergence dates of individual trees vary between species and as a function of local conditions (soil type, topography, etc). In a given landscape, the simultaneous presence of leaf-on and leaf-off conditions is therefore common.

2.2. Drivers and dynamics of biomass in savannahs and woodlands

Although the vegetation types generally follow the precipitation regimes as seen in Fig. 1, a number of other parameters control the regional distribution of forests, savannahs and grasslands and, within savannahs, the local variation in woody cover. It has been shown that the mean annual precipitation (MAP) governs the maximum woody cover in African savannahs; however the actual woody cover, and therefore the biomass, is regulated below the MAP-controlled upper bound by soil properties, topography, and disturbances such as fire, herbivory (Sankaran et al., 2005) or human-induced disturbances such as clearing and logging. Below 650 $mm \cdot yr^{-1}$, the maximum woody cover is constrained by MAP and increases linearly with it, resulting in a “stable” savannah state, but above 650 $mm \cdot yr^{-1}$, the maximum woody cover reaches the woody canopy closure (about 80% tree cover) and the vegetation type can be a closed forest or a savannah depending on the occurrence of disturbances (fire, herbivory). Savannahs and forests are therefore alternative biome states in large parts of Africa (Hirota et al., 2011; Staver et al., 2011).

The causes of change in the biomass of African savannahs are mostly anthropogenic, either directly, *e.g.* through land-use change and forestry (LUCF) and agriculture, use of fire and grazing of domesticated animals, or indirectly, *e.g.* through climate change. More than half of the African population live in these ecosystems and largely depend on them for their livelihoods, through activities such as subsistence farming, livestock grazing, timber production and the extraction of fuel wood (Chidumayo and Gumbo, 2010), all of which have direct impacts on the carbon stocks. At the same time, the impact of these human activities is poorly estimated: for example, reported deforestation rates and changes in croplands are highly variable (Houghton and Hackler, 2006). Most of these direct human activities lead to carbon losses, but carbon gains are also widespread (Bodart et al., 2013), for example in the form of woody encroachment. The drivers of woody encroachment are complex and related to human activities, through grazing density and changes in fire regimes, but also to climate change, through increased atmospheric CO2 concentration, which improves the competitiveness of C_3 trees over C_4 grasses (Bond and Midgley, 2012), and rainfall (O'Connor et al., 2014). The carbon gains brought by woody encroachment are not necessarily considered as positive outcomes by the local populations, who suffer from a reduced grazing capacity with cascading effects on ecosystem services and rural livelihood maintenance (Eldridge et al., 2011).

Because these drivers of AGB changes are complex and intertwined, and can result locally in carbon losses or gains, predictions on the evolution of carbon stocks in Africa in the near future are extremely uncertain. This reinforces the need of direct large-scale monitoring activities, such as AGB estimation based on remote sensing observables.

3. Data

3.1. Field data

3.1.1. Field data selection

In order to train a model that relates PALSAR intensities to AGB, we use AGB estimates derived from field measurements, from several campaigns carried out in different countries in Africa between 2000 and 2013, both from published literature and from original campaigns. To increase the reliability of the model, it is necessary to reduce as much as possible the perturbations that affect the relationship between the SAR backscatter and the AGB estimates. The error sources include firstly mismatches between the size of the field plots and the pixel size of the SAR images (Réjou-Méchain et al., 2014), tree canopy layover and border effects, errors in data geolocation, and topographic effects. In order to minimize these errors, we decided to consider only *in situ* AGB plots with a size larger than 0.25 ha and located in flat areas (mean slope lower than 5°). This first selection step ensures both higher plot homogeneity and lower noise in the radar backscattering.

Georeferenced polygons were available for 1 ha plots in Cameroon from the REDDAF (Reducing Emissions from Deforestation and Degradation in Africa) project (Haeusler et al., 2012), and in South Africa from the Council for Scientific and Industrial Research (CSIR), and the SAR intensities were averaged over these polygons. For other plots only the coordinates of the centre of the plots were available. In this case, as the field plots were bigger than the pixel size, the SAR intensities have been calculated on a 3 × 3 pixels neighbourhood centred on each plot. A test was then applied to keep only the plots that were located in a homogeneous area of the SAR mosaic. This test consisted in discarding the field plots for which the coefficient of variation (CV) of the SAR intensities in the considered 3 × 3 pixels neighbourhoods was higher than 0.25. This threshold is a trade-off between the need to discard heterogeneous plots and the need to keep a sufficient number of plots for a reliable training of the model.

In total, 144 field plots were selected, located in 8 countries (Cameroon, Burkina Faso, Malawi, Mali, Ghana, Mozambique, Botswana and South Africa), with a mean plot size of 0.89 ha. The field data collection period spreads between 2006 and 2012, with a distribution averaging 2010 ± 2.5 year. The selected *in situ* data characteristics are summarized in Table S1.

In each field plot, the AGB has been estimated by applying allometric equations to *in situ* measurements of tree parameters (diameter at breast height, tree height, basal area), following proper sampling methodologies. The corresponding allometric equations and methodologies are described in the references cited in Table S1. Among the studies that use the allometries described in Chave et al. (2005), the "dry forest" equation is used for savannah species and the "moist forest" for forest species.

3.1.2. Field data uncertainties

In situ AGB estimates are affected by a number of error sources, including field measurement errors (diameter at breast height, tree height), estimate of wood density and allometric models (Chave et al., 2004). An error of 10% was reported for the wood density and an error of 5% for the allometric equations by Chave et al. (2004), while the errors related to diameter at breast height and tree height measurements were estimated to be 2.25% and 4.47% respectively in a previous study (Mermoz et al., 2014). The errors were propagated by Monte Carlo simulations to yield a standard deviation associated with plot-based AGB estimates, in the plots measured in Cameroon and South Africa in 2012 and 2013 (plots 72 to 144 in Table S1). This approach yielded a mean field measurement error of σ_M = 5.2% in Cameroon and σ_M = 9.7% in South Africa. A trade-off error of σ_M = 7% was associated to the other plots, for which we did not have access to the individual tree measurements that allow the direct estimation of σ_M through the computation of Monte-Carlo simulations. The sampling errors σ_S associated with the mismatch in spatial scales between the field plots and the pixel size was estimated for each plot using Fig. S10 published in Réjou-Méchain et al. (2014), with a 9% mean error.

The field measurement error σ_M and sampling error σ_S were combined by adding the associated standard deviations quadratically, to obtain the overall field data uncertainties at the plot level:

$$\sigma_{AGB\ field} = \sqrt{\sigma_M^2 + \sigma_S^2} \quad (1)$$

3.2. SAR data

3.2.1. SAR data description

The global dual polarisation (HH, HV) 25 m resolution ALOS PALSAR mosaic produced by JAXA for the year 2010 was used in this study. The mosaic consists of a collage of Fine Beam Dual-polarisation (FBD) data strips acquired in ascending mode with HH and HV polarizations. For each pixel, the mosaic dataset also includes values of the local incidence angle and acquisition date. The FBD data have a swath width of about 70 km. To cover the African continent, about 180 data strips have been used. About 91% of the data have been acquired in 2010, between 1 May and 28 November, and the remaining gaps have been filled with FBD imagery from 2009 and 2008. The data have been processed by JAXA using the large-scale mosaicking algorithm described in Shimada and Ohtaki (2010), including ortho-rectification, slope correction and radiometric calibration between neighbouring strips.

The digital numbers (DN) were converted into γ^o values using the following equation:

$$\gamma^o(dB) = 10\log_{10}(DN^2) + CF \quad (2)$$

where *CF* is a calibration factor equal to − 83.0 dB, as provided in Shimada et al. (2009). In order to reduce the SAR backscatter uncertainty related to the speckle noise, we applied a multi-image filter developed by Bruniquel and Lopes (1997) and Quegan and Yu (2001) to decrease the speckle effect while preserving the spatial resolution of the images. The 2007, 2008, 2009 and 2010 PALSAR mosaics at HH and HV polarizations (8 images) were used as inputs to the filter. The mosaic is generated with an equivalent number of looks (ENL) of 16. After filtering, the theoretical ENL value is 112 using a 7 × 7 window. This corresponds to a decrease of SAR backscatter uncertainty due to speckle from 1.6 dB to 0.5 dB for a − 25 dB backscatter, and from 1.2 dB to 0.4 dB for a − 7 dB backscatter (See Section 3.2.3).

3.2.2. Issues related to data homogeneity in large mosaics composed of multi-date acquisitions

When applying a single inversion scheme to radar data acquired at different dates, as is the case in the PALSAR mosaic, sources of error include variations of environmental effects between acquisition strips (soil and vegetation moisture, leaf-on/leaf-off and grass/understory conditions, *e.g.* if images are acquired during different seasons) and, less importantly, radar backscatter variation caused by radar calibration and incidence angle variation in a data strip. As a result, sharp radiometric discontinuities can be observed between adjacent PALSAR strips when the mosaics are produced. These discontinuities, although they locally represent the reality of the backscatter at the time of the acquisitions, are considered troublesome for large-scale applications based on the mosaics. To reduce this problem, inter-strip balancing algorithms were applied by JAXA in order to equalize the backscatter across the whole mosaics (Shimada and Ohtaki, 2010). In addition, the seasonal effects were further minimised by the fact that, thanks to the ALOS systematic observation strategy, most of the data (74% in Africa, and 80% if Western Sahara is excluded) has been acquired within a four-month period between June and September (Fig. 2, left). During this period, Africa is subject to a wet season regime mostly in its northern hemisphere, up to approximately 15° north. In the rest of the

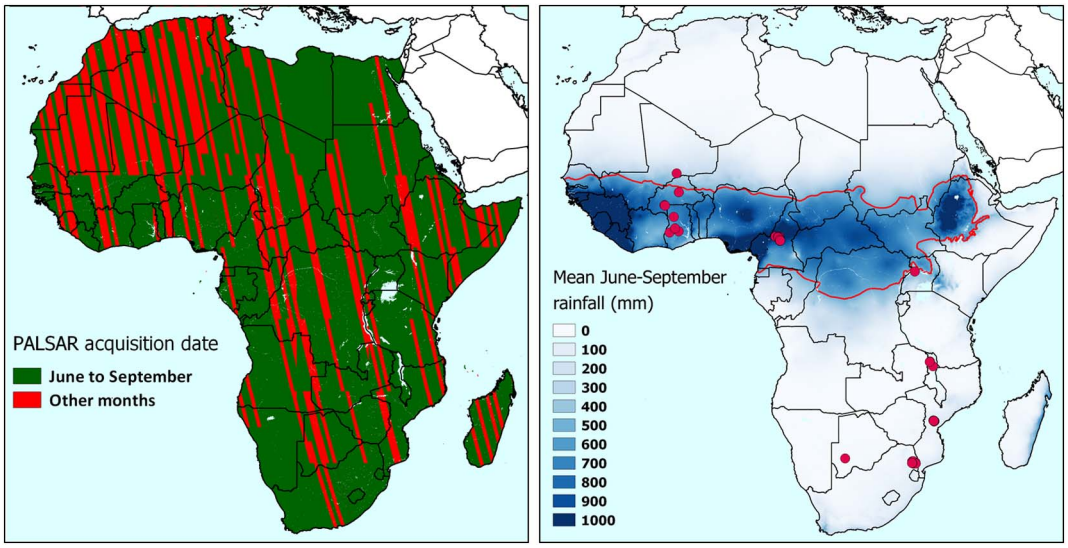

Fig. 2. (Left) Acquisition dates of the 2010 PALSAR mosaic (green: June to September; red: other months), and (Right) Precipitations from Worldclim aggregated from 1950 to 2000 between June and September, together with the location of the selected forest inventory plots (red disks) and the 500 mm isoline used to separate wet and dry season areas where two different backscatter-AGB models are developed (red line). (For interpretation of the references to color in this figure legend, the reader is referred to the web version of this article.)

continent, *i.e.* Northern, Southern and Eastern Africa, this period corresponds to a dry season, with very low rainfall. During the dry season, the soil moisture is consistently low and most trees have lost their leaves, which minimizes discrepancies between strips and increases the sensitivity of the backscatter-AGB relationships (Mathieu et al., 2013; Urbazaev et al., 2015). In the wet season, the vast majority of trees have their leaves on, but the random occurrence of rainfall events leads to locally reduced sensitivity in the backscatter-AGB relationship as well as larger inter-strip variations. As a consequence, we decided to estimate the AGB separately in dry season areas and in wet season areas, keeping in mind that better results should be found in the dry season. The delimitation between dry and wet season areas is set by a rainfall isoline corresponding to a mean total rainfall of 500 mm over the June–September period (Fig. 2, right), calculated from rainfall data of the WorldClim database (http://www.worldclim.org) representative of the 1950–2000 period (Hijmans et al., 2005).

3.2.3. SAR data uncertainties

The errors impacting the estimation of SAR backscatter can be decomposed into two terms: radiometric accuracy and radiometric resolution. Whereas the former expresses the mean difference between the measured and the true value (usually from an *ad-hoc* calibration target), the latter characterizes the stability of the observations, and is mainly governed by the speckle effect, and therefore by the number of looks. Assuming that radiometric accuracy is stable and does not depend on the spatial location, this component can be considered as a simple shift, with no impact in this study. We therefore focus on the effect of the radiometric resolution, which can be expressed as a function of the coefficient of variation of the SAR backscatter (Massonnet and Souyris, 2008):

$$CV = \frac{\sigma_{SAR}}{\mu_{SAR}} = \frac{1 + SNR^{-1}}{\sqrt{ENL}} \quad (3)$$

where μ_{SAR} represents the mean SAR backscatter in linear scale, σ_{SAR} represents its standard deviation, and SNR represents the signal-to-noise ratio, which is defined as the ratio between the measured backscatter and the NESZ (Noise Equivalent Sigma Nought).

We can therefore express the SAR backscatter uncertainty under the following form:

$$\sigma_{SAR} = \frac{\mu_{SAR} + \mathrm{NESZ}}{\sqrt{ENL}} \quad (4)$$

In our case, Eq. (4) can be applied at the pixel level, considering the local backscatter, an overall NESZ of -32 dB for PALSAR FBD data (Shimada et al., 2009) and a number of looks equals to 112. This SAR backscatter uncertainty, when transformed in dB, is higher for the lower backscatter values and ranges between about 0.5 dB and 0.42 dB for backscatter values of -25 dB and -7 dB respectively.

4. Development of the inversion scheme

4.1. Approach

The relationship between the radar backscatter and AGB is complex and depends on a large number of parameters related to vegetation (forest structure, vegetation water content, presence/absence of leaves) and to the ground (soil moisture, soil roughness, topography), collectively designated as “environmental conditions”. The lack of suitable datasets available globally at sufficient resolutions makes it virtually impossible to estimate AGB from the backscatter by taking into account these environmental conditions explicitly.

In this study, the approach that we use consists in performing the AGB estimation separately in the “wet season areas” and in the “dry season areas” described in Section 3.2.2, such as most of the backscatter variability is minimised with respect to the most important factors. A simple model is developed, representing the relationship between the backscatter and AGB for the average environmental conditions encountered in each area: leaf-on, wet soil, and high vegetation water content in the “wet season areas”, and leaf-off, dry soil, and lower vegetation water content in the “dry season areas”. The variability of the backscatter, caused by potential deviations from these average environmental conditions, is simulated using an electro-magnetic model (Villard, 2009) and is used in the Bayesian inversion of the simple model.

4.2. Analysis of backscatter versus biomass

The sensitivity of the radar backscatter to AGB is analysed using the 2010 ALOS mosaic and *in situ* AGB data. Fig. 3. shows the backscatter data (γ^0_{HH} and γ^0_{HV}) as a function of the AGB of the *in situ* plots, where *in situ* plots located in the wet season areas and dry season areas, as defined in Section 3.2.2, are plotted in blue and red respectively. As expected, we found that the relationship between the radar backscatter and AGB depends on wet and dry season areas. Note that for the wet

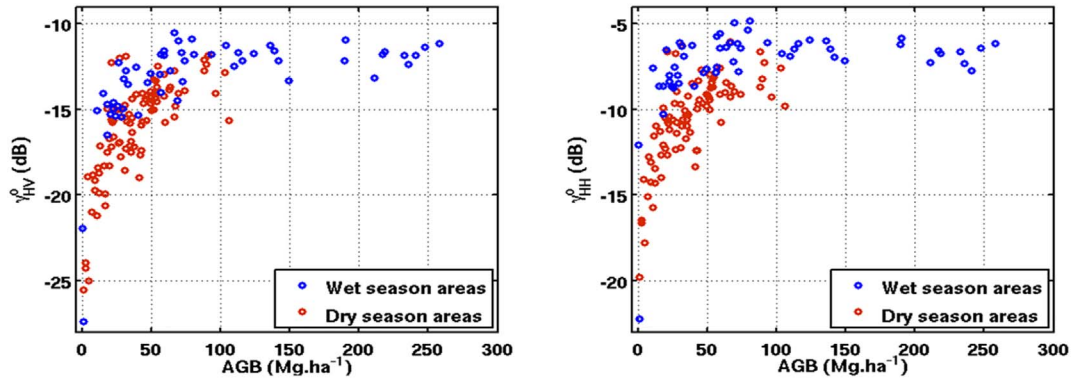

Fig. 3. ALOS backscatter (γ^0_{HV} and γ^0_{HH}) from mosaic data acquired in 2010 *versus in situ* AGB estimated over 144 plots in wet and dry season areas. The dynamic range of backscatter is lower in the wet season than in the dry season because higher soil moisture increases the radar backscatter over bare soils.

season areas, *in situ* plots cover a larger range of AGB (up to 250 Mg·ha^{-1}), whereas for the dry season areas, *in situ* AGB is under 120 Mg·ha^{-1}. In the range of AGB under 100 Mg·ha^{-1}, as expected, the backscatter is mostly higher in wet season areas, which is explained by the higher soil and vegetation wetness, and probably also by the vegetation structure and phenology (leaf-on). However, the dynamic range of backscatter is lower in the wet season (about 3 dB and 4 dB from 10 to 150 Mg·ha^{-1} for HH and HV respectively) than in the dry season (about 7 dB and 9 dB for HH and HV respectively), because lower soil moisture decreases the radar backscatter from the ground and grass-dominated areas. This justifies our choice to derive two different models in the regions where the PALSAR data was acquired in the wet season and in the dry season.

4.3. The model relating ALOS PALSAR to AGB

In general, the backscatter from a forest canopy is mainly governed by scattering mechanisms from the vegetation, and from the bare ground and underlying ground attenuated by the vegetation layer, plus the coupling terms between ground and vegetation, commonly referred to as double bounce scattering mechanism. The relative contribution of each scattering mechanism in the backscatter depends on the radar frequency, polarisation, incidence angle, the environment conditions (soil moisture, surface roughness, topography) and the vegetation characteristics (AGB, structure, moisture content).

The radar backscatter is sensitive to forest AGB through vegetation scattering, through the wave attenuation by the vegetation, and through the double bounce. One possible approach to characterize the relationship between backscatter and AGB consists in retaining the main scattering mechanisms in a simplified backscatter formulation, and comparing the formulation with the empirical data. The comparison will give information on the validity of the simplification.

One common formulation is a 3-parameter semi-empirical equation which consists in a sum of the ground (a) and vegetation (b) contributions weighted by the attenuation caused by different vegetation layers ($e^{-\mathbf{c}.AGB}$):

$$\gamma^0 = a \cdot e^{-\mathbf{c}.AGB} + b \cdot (1 - e^{-\mathbf{c}.AGB}) \quad (5)$$

This formulation corresponds to the modified Water Cloud Model (Santoro et al., 2002), an adaptation of the original Water Cloud Model (Attema and Ulaby, 1978) widely used at higher frequencies like C-band, except that the stem volume is replaced by the biomass. This 3-parameter model has already been used for L-band data by several authors (Cartus et al., 2012; Mermoz et al., 2014; Michelakis et al., 2014; Mitchard et al., 2011). For such long wavelengths however, attenuation is significantly less important than at C-band so that the effects of ground scattering are more important, whether through its direct contribution or through the double bounce contribution, especially in open landscapes like savannahs. In order to introduce this double bounce explicitly in Eq. (5), one can consider the following expression:

$$\gamma^0 = (a + d) \cdot e^{-\mathbf{c}.AGB} + b \cdot (1 - e^{-\mathbf{c}.AGB}) \quad (6)$$

based on the assumptions that scattering mechanisms are independent and that in the monostatic configuration, the double bounce contribution (noted d) can be projected onto the ground (Villard and Borderies, 2015).

It is worth stressing that, unlike the ground and vegetation parameters (a, b) which can be reasonably assumed independent of the AGB for low biomass forests, the double bounce parameter (d) is actually a function of AGB, but also of forest structure and especially forest closure/openness. As an example, for the same AGB, the double bounce contribution in HV can be significant in the case of sparsely distributed trees with developed canopies, but almost null in the case of densely distributed trees with few branches. With this respect, d and c can be linked since forest closure also impacts attenuation. Despite this complexity, we can easily demonstrate that Eq. (6) is equivalent to Eq. (5) if parameter c is replaced by an effective parameter $c_{eff} = c - \frac{1}{AGB} ln\left(\frac{a+d-b}{a-b}\right)$. Beyond the mathematical trick, the physical interpretation of Eq. (5) is now that c does not govern only attenuation but also the double bounce scattering mechanism. This is also consistent with the fact that c governs the growth rate of γ^0, since the dispersion in the backscatter is mainly due to the possible double bounce for a given biomass.

This justifies our choice to keep the simple expression of Eq. (5) as our regression model, and to use simulations from an electro-magnetic model to account for the dispersion around the expected mean backscatter in the Bayesian inversion process described in Section 4.5.

4.4. Calibration of the direct model

Different approaches can be used to estimate the three parameters, a, b, and c, required for Eq. (5). Regarding the parameters a and b, we can use statistical regressions between the SAR data and *in situ* plot data, provided there are a sufficient number of plots, well distributed over the relevant range of AGB and plot conditions. When the *in situ* plot data do not meet these requirements, parameter a can be estimated from pixels corresponding to bare ground (*i.e.* bare soil or grassy areas) and b from pixels corresponding to closed forests. One option is to use ancillary data such as Landsat tree cover (LTC) continuous field from Sexton et al. (2013), similarly to what was done in Cartus et al. (2014). Mean values of backscatter from pixels corresponding to LTC values of 0% (or lower than a threshold) and 100% (or higher than a threshold) crown cover are used as proxy for estimating parameters a and b. This approach is however expected to provide better results for the estimation of parameter b than for parameter a, as the low canopy pixels in the LTC dataset will tend to incorporate, in addition to the targeted bare soil or grassy areas, low shrub areas which can have a significant woody

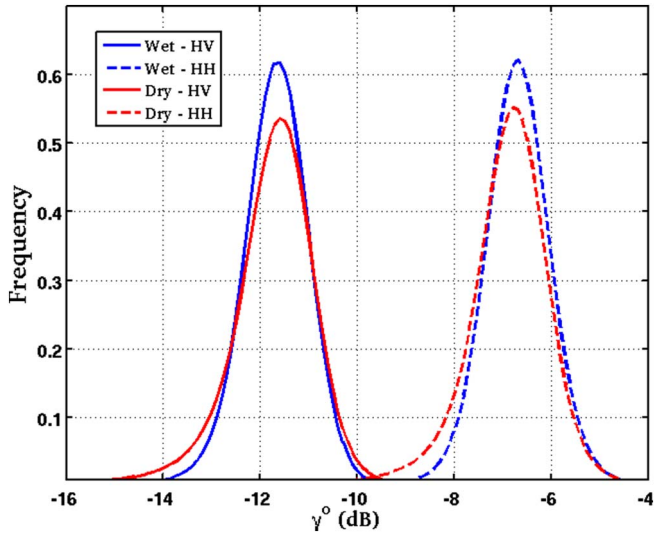

Fig. 4. Distribution of HV and HH backscatters acquired in the wet season and dry season areas in sub-Saharan Africa, over values of Landsat tree cover continuous field (Sexton et al., 2013) larger than 90%.

biomass. Parameter *c*, which represents the vegetation attenuation, varies as a function of vegetation water content and vegetation structure (vertical and horizontal distribution of scatterers, number of stems per hectare, *etc.*). Hence *c* changes with forest type and must be derived using *in situ* AGB plot data.

In this study, we had a sufficient amount of low AGB plots (below 25 Mg·ha^{-1}) to accurately calibrate parameter *a*. However, there was a lack of high AGB plots (above 150 Mg·ha^{-1}) to estimate properly parameter *b*, especially for the dry conditions. Thus, we extracted separately for each region the backscatter values over values of LTC larger than 90%, to pick up the "dense forest" pixels only. The probability density functions of γ^0_{HV} and γ^0_{HH} over dense forests are plotted in Fig. 4. The mean and standard deviations are -6.68 ± 0.69 dB for γ^0_{HH} and -11.59 ± 0.65 dB for γ^0_{HV} acquired during wet conditions and -6.76 ± 0.82 dB for γ^0_{HH} and -11.63 ± 0.83 dB for γ^0_{HV} acquired during dry conditions. These values are consistent with the values obtained from the *in situ* plots in the wet season areas, as can be seen in Fig. 5. It can be noted that for closed canopy, small difference in the backscatter is found between wet and dry season. This tends to indicate that the *b* parameter is not sensitive to environmental conditions and could therefore be estimated jointly in the dry and wet season areas.

After estimating parameter *b*, parameters *a* and *c* have been estimated using statistical regressions between the SAR data and *in situ* plot data. Table 1 summarises the values of the parameters *a*, *b*, and *c*, together with the Pearson correlation coefficient (ρ) and Root Mean Square Difference (RMSD) of the backscatter-AGB regressions on the 0-100 Mg·ha^{-1} biomass range, for the wet season areas and the dry season areas and for the case where we do not take into account this seasonality. In Eq. (5), the backscatter γ^0 is expressed in linear values, and therefore parameters *a* and *b* as well, but we give only the corresponding dB values in Table 1 as they are more easily understood. Parameter *a* differs between wet and dry season by 0.6 dB in HH and 0.8 dB in HV, and parameter *c* changes significantly between wet and dry season, for both HH and HV. This experimental result indicates that for the backscatter at L-band of savannah and woodlands, a first assumption that could be made is that the effect of tree structure is less important than the moisture effect. The correlation coefficient and RMSD values confirm the relevance of our approach which consists in separating wet and dry season areas, as it reduces the backscatter dispersion (RMSD) and increases the correlation (especially for HV) compared to the case where seasonality is not taken into account.

Fig. 5 shows the corresponding regression curves as well as the 144 field plots with their corresponding field and SAR data uncertainties $\sigma_{AGB\ Field}$ and σ_{SAR}, represented as error bars along the x and y axis respectively.

4.5. Bayesian inversion of the model

In order to minimize the error propagation which would result from the direct use of Eq. (5) to convert γ^0 into AGB, a Bayesian approach is preferred, as proposed in previous studies related to model parameter estimations (Notarnicola and Posa, 2004; Tarantola, 2005).

Note that in this section, we use simplified expressions of the probability density functions, where $\gamma_{HH}{}^0 = \gamma_{HH\ obs}{}^0$ is replaced by $\gamma_{HH\ obs}{}^0$, $\gamma_{HV}{}^0 = \gamma_{HV\ obs}{}^0$ is replaced by $\gamma_{HV\ obs}{}^0$, and AGB = B is replaced by B.

The Minimum Mean Square Error (MMSE) estimator of AGB is given by the conditional expectancy:

$$\mathrm{AGB}_{est} = E[\mathrm{AGB} \mid \gamma^0_{HH\ obs}, \gamma^0_{HV\ obs}] = \int_0^{AGB_{max}} \mathrm{B}.\ p(\mathrm{B} \mid \gamma^0_{HH\ obs}, \gamma^0_{HV\ obs})\, dB \quad (7)$$

where E[*X*] represents the expected value of X. The inversion therefore requires the calculation of the posterior probability $p(\mathrm{B} \mid \gamma_{HH\ obs}{}^0, \gamma_{HV\ obs}{}^0)$ of AGB given the observation $(\gamma_{HH\ obs}{}^0, \gamma_{HV\ obs}{}^0)$, which is obtained using Bayes' theorem:

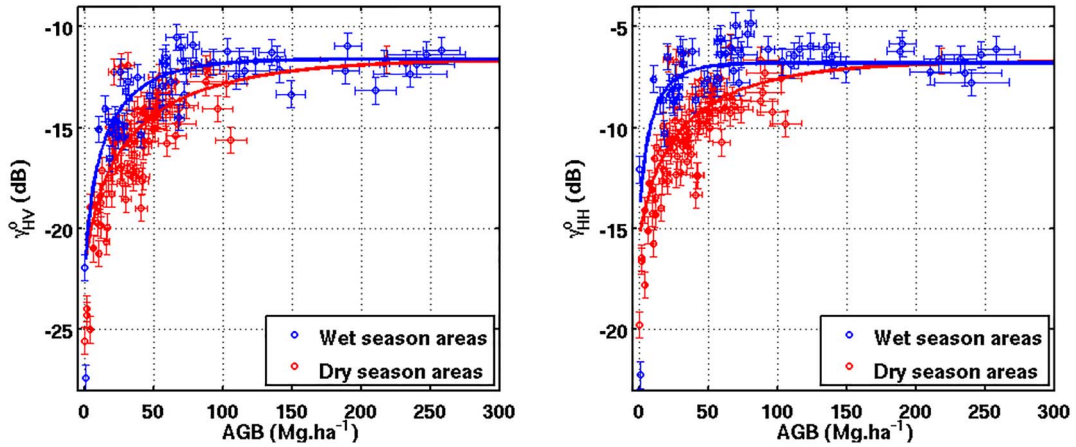

Fig. 5. ALOS backscatter (γ^0_{HV} and γ^0_{HH}) from mosaic data acquired in 2010 versus in situ AGB estimated over 144 plots in African wet and dry season areas, with the regression curves corresponding to the calculated direct model, together with field uncertainties $\sigma_{AGB\ field}$ (described in Section 3.1.2) and SAR uncertainties σ_{SAR} (described in Section 3.2.3) associated to each field plot.

Table 1
Parameters of the direct model relating ALOS PALSAR to AGB.

	HH			HV		
	Wet	Dry	All	Wet	Dry	All
a	− 14.9 dB	− 15.5 dB	− 16.4 dB	− 22.8 dB	− 22.0 dB	− 23.2 dB
b	− 6.7 dB	− 6.8 dB	− 6.8 dB	− 11.6 dB	− 11.6 dB	− 11.6 dB
c (ha·Mg^{-1})	0.0616	0.0154	0.0249	0.0291	0.0129	0.0174
ρ	0.64	0.68	0.62	0.77	0.71	0.64
RMSD	1.80 dB	1.54 dB	1.98 dB	1.43 dB	1.67 dB	1.78 dB

$$p(B \mid \gamma^0_{HH\ obs},\ \gamma^0_{HV\ obs}) = \frac{p(\gamma^0_{HH\ obs},\ \gamma^0_{HV\ obs} \mid B)p(B)}{p(\gamma^0_{HH\ obs},\ \gamma^0_{HV\ obs})} \quad (8)$$

Three terms need to be assessed. The marginal likelihood $p(\gamma_{HH\ obs}{}^0,\ \gamma_{HV\ obs}{}^0)$ is constant in the scene and is therefore neglected, as a normalization factor will be applied (see Eq. (11)).

The prior probability, p(B), corresponds to the distribution of AGB in the scene. This distribution is unknown in most cases, and its probability density function is therefore considered uniform over the [0 AGB_{max}] range, where AGB_{max} represents the assumed highest biomass in savannahs and woodlands of Africa. By analysing the distribution of AGB obtained from Saatchi et al. (2011) across the areas of savannahs and woodlands identified in Africa from the ESA Climate Change Initiative (CCI) Land Cover 2010 map (http://www.esa-landcover-cci.org/), we found that a reasonable estimate of AGB_{max} is 100 Mg·ha^{-1}.

The likelihood function $p(\gamma_{HH\ obs}{}^0,\ \gamma_{HV\ obs}{}^0 \mid B)$ accounts for the dispersions of HH and HV backscatters caused by environmental conditions and forest structure, for a given AGB value. These dispersions are considered at a first approximation independent in HH and HV, and the joint conditional probability density function can thus be expressed as the product of the individual conditional probability density functions:

$$p(\gamma^0_{HH\ obs},\ \gamma^0_{HV\ obs} \mid B) = p(\gamma^0_{HH\ obs} \mid B) \cdot p(\gamma^0_{HV\ obs} \mid B) \quad (9)$$

For a given biomass value B, the estimation of the probability density function $p(\gamma_{obs}{}^0 \mid B)$ for each polarisation requires two steps.

First, we estimate the theoretical backscatter $\gamma_{theo}{}^0$ by inverting the model from Eq. (5). Second, we express the probability that the observed backscatter $\gamma_{obs}{}^o$ deviates from this theoretical backscatter $\gamma_{theo}{}^0$ because of potential environmental effects (soil moisture, vegetation structure, phenology). We model the probability of $\gamma_{obs}{}^o$ using a Gaussian distribution characterized by a mean value equal to $\gamma_{theo}{}^o$, and a standard deviation σ_{simu} estimated by simulation results from the MIPERS (Multistatic Interferometric Polarimetric Electro-magnetic model for Remote-Sensing) model (Villard, 2009). This σ_{simu} term models the variability of $\gamma_{theo}{}^0$ with environmental conditions (soil and vegetation moisture, presence or absence of leaves) and forest structure. The forest growth model used to feed the geometrical parameters to the MIPERS model is fully described in Mermoz et al. (2015) and is calibrated using the *in situ* data available in this study. Assumptions are made to define the range of values of other required MIPERS inputs, such as soil and vegetation moisture, soil roughness *etc.* We vary the MIPERS inputs and propagate these variations by Monte Carlo simulations to obtain the standard deviation σ_{simu}. Note that σ_{simu} is not constant and varies with AGB. Higher values are associated to low AGB ($\gamma_{theo}{}^o$ being very dependent on the environmental conditions) and lower values are associated to high AGB ($\gamma_{theo}{}^o$ is more stable over dense forests than over bare soils). For a given $\gamma_{obs}{}^o$, the likelihood function $p(\gamma_{obs}{}^0 \mid B)$ is therefore estimated for each polarisation as follows:

$$p(\gamma^0_{obs} \mid B) = \frac{1}{\sqrt{2\pi}\ \sigma_{simu}(B)} e^{-\frac{1}{2}\left(\frac{\gamma^0_{obs}-\gamma^0_{theo}(B)}{\sigma_{simu}(B)}\right)^2} \quad (10)$$

Combining Eqs. (8) to (10) leads to the following expression of the posterior probability:

$$p(\mathrm{B} \mid \gamma^0_{HH\ obs}, \gamma^0_{HV\ obs}) = K \frac{e^{-\frac{1}{2}\left(\frac{\gamma^0_{HH\ obs}-\gamma^0_{HH\ theo}(B)}{\sigma_{HH\ simu}(B)}\right)^2}}{\sigma_{HH\ simu}(B)} \frac{e^{-\frac{1}{2}\left(\frac{\gamma^0_{HV\ obs}-\gamma^0_{HV\ theo}(B)}{\sigma_{HV\ simu}(B)}\right)^2}}{\sigma_{HV\ simu}(B)} \quad (11)$$

where K is a normalization factor, which includes the multiplicative factors that have been removed from Eqs. (8) and (10).

The mode of the posterior probability density function described in Eq. (11) gives the maximum likelihood estimate of AGB, *i.e.* the most likely value of AGB for a given observation and for a uniform distribution of AGB. In this study, we prefer to retain the AGB estimate obtained by the MMSE estimator given in Eq. (7) in order to minimize the overall error in the dataset.

4.6. Post-processing of AGB estimates

The method described in Sections 4.2 to 4.5 is applied to the 2010 PALSAR mosaic data over Africa, independently over the dry season and wet season areas. While the maximum AGB value used to define the prior probability p(B) in the Bayesian scheme is equal to 100 Mg·ha^{-1}, as mentioned in Section 4.5, the resulting AGB values estimated through the Bayesian inversion (MMSE estimator) never exceed 85 Mg·ha^{-1}. Because AGB estimates in the range of 0 to 85 Mg·ha^{-1} would yield large errors in some biomes like dense forests, the inversion should better be restricted to the savannah and woodland ecosystems. One potential way of doing this could be to invert pixel values into AGB with the direct model and mask out pixels with an AGB higher than 100 Mg·ha^{-1}. However, as was evidenced in Mermoz et al. (2015), backscatter coefficients over forest plots of > 150 Mg·ha^{-1} can decrease when the forest becomes a dense medium. AGB of such forest pixels will be underestimated in the model-based inversion, resulting in the failure of this approach.

Two options have been identified to overcome this problem. The first option is to lower the AGB threshold value above which pixels are masked out, in order to effectively discard all the dense forest pixels. A drawback of this approach is that it lowers the value of the maximum estimated biomass (approximately 70 Mg·ha^{-1} following Mermoz et al., 2015, instead of approximately 85 Mg·ha^{-1} in this study). In other terms, this would exclude all dense forests, but would also exclude the highest range of savannah and woodland biomass. Instead, we chose a more straightforward solution which uses independent sources of information, such as land cover maps, to mask out dense forest areas. Among the available land cover maps in Africa, the Global land cover (GLC) 2000 map (Mayaux et al., 2004), which is based on SPOT-VEGETATION data, has a resolution of 1 km. The GlobCover 2009 (Arino et al., 2012) and the CCI Land Cover 2010 map have a resolution of 300 m. From these maps, we selected the most recent CCI Land Cover 2010 map. In this map, we considered as dense forest the class *Broadleaved evergreen closed to open forest.* We also used the CCI Land Cover 2010 map to mask out flooded forests, mangroves, urban areas and water bodies. The GLC 2000 map was used to mask out some bare areas embedded with rocks that lead to false-alarms in AGB detection, for example in Southern Algeria or in Northern Chad, as these areas are not

accounted for in the CCI Land Cover 2010 map.

The pre-processed and filtered 2010 PALSAR mosaic data at 25 m resolution, where the dense forest, flooded forests, mangroves, urban areas, bare rocks and water bodies have been excluded, have been inverted on a pixel basis into AGB values using the Bayesian inversions for dry and wet conditions. To avoid AGB discontinuities between the dry and wet regions, we used a fuzzy approach so that pixels can be assigned grades of membership to the dry and wet parts in a fuzzy set from zero to one, in a two-degree-wide buffer surrounding the 500 mm rainfall isolines. The membership function we used is a S-shaped spline-based curve:

$$f(x) = \begin{cases} 0, & x < -2 \\ \frac{(x+2)^2}{8}, & -2 \le x < 0 \\ 1 - \frac{(x-2)^2}{8}, & 0 \le x \le 2 \\ 1, & x > 2 \end{cases} \quad (12)$$

where x represents the distance (in degrees) to the 500 mm rainfall isoline.

4.7. Uncertainties assessment

4.7.1. Accuracy

As the true AGB is unknown, the accuracy at each pixel, which is defined by how close the estimated AGB is to the true AGB, cannot be directly assessed. However, within the Bayesian inversion scheme, the accuracy of the estimates can be approached by calculating credible intervals, which represent the range of likely values of AGB under the retained assumptions related to the variability of the backscatter with environmental conditions (modelled with σ_{simu}) and to the range of AGB values in the savannahs and woodlands areas (0 to 100 Mg·ha^{-1}).

In this study, we choose the 95% highest posterior density interval (95% HPDI), which is commonly used in Bayesian statistics. It is defined by the narrowest interval [B_{min} B_{max}] that contains the true AGB value with a 95% probability, and therefore verifies:

$$\int_{B_{min}}^{B_{max}} p(B \mid \gamma^0_{HH\ obs}, \gamma^0_{HV\ obs}) dB = 0.95 \quad (13)$$

The width of this 95% HPDI is a measure of the error that we make in our AGB retrieval scheme by not taking into account the environmental conditions explicitly (*i.e.* at each pixel with ancillary data). It can be used as a proxy of the accuracy of the AGB estimates that are produced in this study.

4.7.2. Precision

The precision of the estimated AGB, which refers to how close the agreement is between repeated estimates, is linked to the precision of all the measurements involved in the Bayesian inversion scheme, *i.e.* the *in situ* AGB measurements and the SAR data measurements.

The precision of the *in situ* AGB measurements is represented by the standard deviation value $\sigma_{AGB\ field}$ calculated for each *in situ* plot, following Eq. (1) and the methodology described in Section 3.1.2. The precision of the SAR data measurements is defined by the standard deviation value σ_{SAR} calculated for each HH and HV backscatter value, following Eq. (4).

These uncertainties linked to the *in situ* AGB estimates and to the SAR data are propagated step-by-step through the whole inversion scheme using a Monte Carlo approach, which allows obtaining the precision of the estimated AGB.

This approach therefore comprises two steps. First, the direct model parameters (a and c) are estimated 1000 times by drawing randomly the AGB, γ^0_{HV} and γ^0_{HH} values of each of the 144 fields according to Gaussian distributions defined by the $\sigma_{AGB\ field}$ and σ_{SAR} standard deviations.

Then, for a given observation characterized by $\gamma^0_{HV\ obs}$ and $\gamma^0_{HH\ obs}$, the standard deviation of the estimated biomass, $\sigma_{AGB\ est}$, is calculated after 1000 iterations of the AGB estimator from Eq. (7), where $\gamma^0_{HV\ obs}$ and $\gamma^0_{HH\ obs}$ are affected by the standard deviation σ_{SAR} following a Gaussian distribution, with the direct model parameters a and c obtained in the 1000 iterations of the first step.

This value $\sigma_{AGB\ est}$ represents the precision associated with the estimated AGB in a pixel defined by $\gamma^0_{HV\ obs}$ and $\gamma^0_{HH\ obs}$ with the method developed in this study.

4.7.3. Overall uncertainties

The overall uncertainties, taking into account both the accuracy and precision of the AGB estimates, can be calculated by running a Monte Carlo simulation in a similar way as in Section 4.7.2. However, in the second step, instead of calculating the standard deviation of the estimated AGB, the overall uncertainty is assessed by calculating the 95% HPDI using the mean of the posterior probability density functions obtained in the 1000 iterations. This approach provides an extended 95% HPDI that accounts for the uncertainties linked to both accuracy and precision.

5. Results

Because the other large-scale AGB datasets available over Africa (Avitabile et al., 2016; Baccini et al., 2012, 2015; Saatchi et al., 2011) give conflicting estimates in the savannahs and woodlands regions, and because very few inventory plots exist in these areas, it is impossible to provide an overall evaluation of the AGB estimates that we have produced in this study. In order to provide a partial evaluation of our results, the AGB map produced in this study is visually compared with the other datasets in Section 5.1 and some differences are analysed. We then perform a cross-validation of our dataset using the available *in situ* inventory data in Section 5.2.1, and a local validation with independent LiDAR estimates in the lowveld region in South Africa in Section 5.2.2. Finally, the carbon estimates aggregated at the country scale are compared in Section 5.3 with the figures reported by FAO and with the corresponding aggregated estimates provided by the other AGB datasets.

5.1. Visual assessment of the biomass dataset

Fig. 6 shows the AGB map of Africa produced using the approach described in this paper. An uncertainty value is associated with each AGB estimate, using the methodology described in Section 4.7. The four pan-tropical AGB datasets mentioned in the Introduction (Avitabile et al., 2016; Baccini et al., 2012, 2015; Saatchi et al., 2011) are displayed in Fig. 7 for comparison with our AGB dataset.

Fig. 7 shows a clear under-estimation of biomass in savannas in the dataset of Avitable when compared to others, as well as less intermediate values between high and low biomass. For example, biomass stocks estimated in Ethiopia are much larger in the datasets of Saatchi and Baccini than in Avitabile's. Whereas Baccini's dataset shows larger biomass estimates than Saatchi's and Avitabile's in some areas like in Angola, it shows as well less areas of intermediate values (from 40 to 60 t/ha) than Saatchi's dataset, like in Kenya, Somalia and Ethiopia for example. The dataset derived in this study (Fig. 6) shows even more biomass dynamics than Saatchi's dataset, *e.g.* in Somalia.

Figs. 8 and 9 show full-resolution comparisons between the AGB estimates produced from ALOS PALSAR in this study and the four other datasets for three subsets selected across different biomes of Africa. In the forest-savannah transition zone depicted in Fig. 8, it can be seen that the datasets by Saatchi and Baccini have a generally higher biomass in the savannahs than our estimates, which have a range of AGB similar to the dataset by Avitabile. A visual inspection of high-resolution optical imagery available in Google Earth reveals that the very low biomass areas (0–10 Mg·ha^{-1}) depicted in our dataset and in Avitabile's actually correspond to treeless areas. Therefore, the datasets of Saatchi

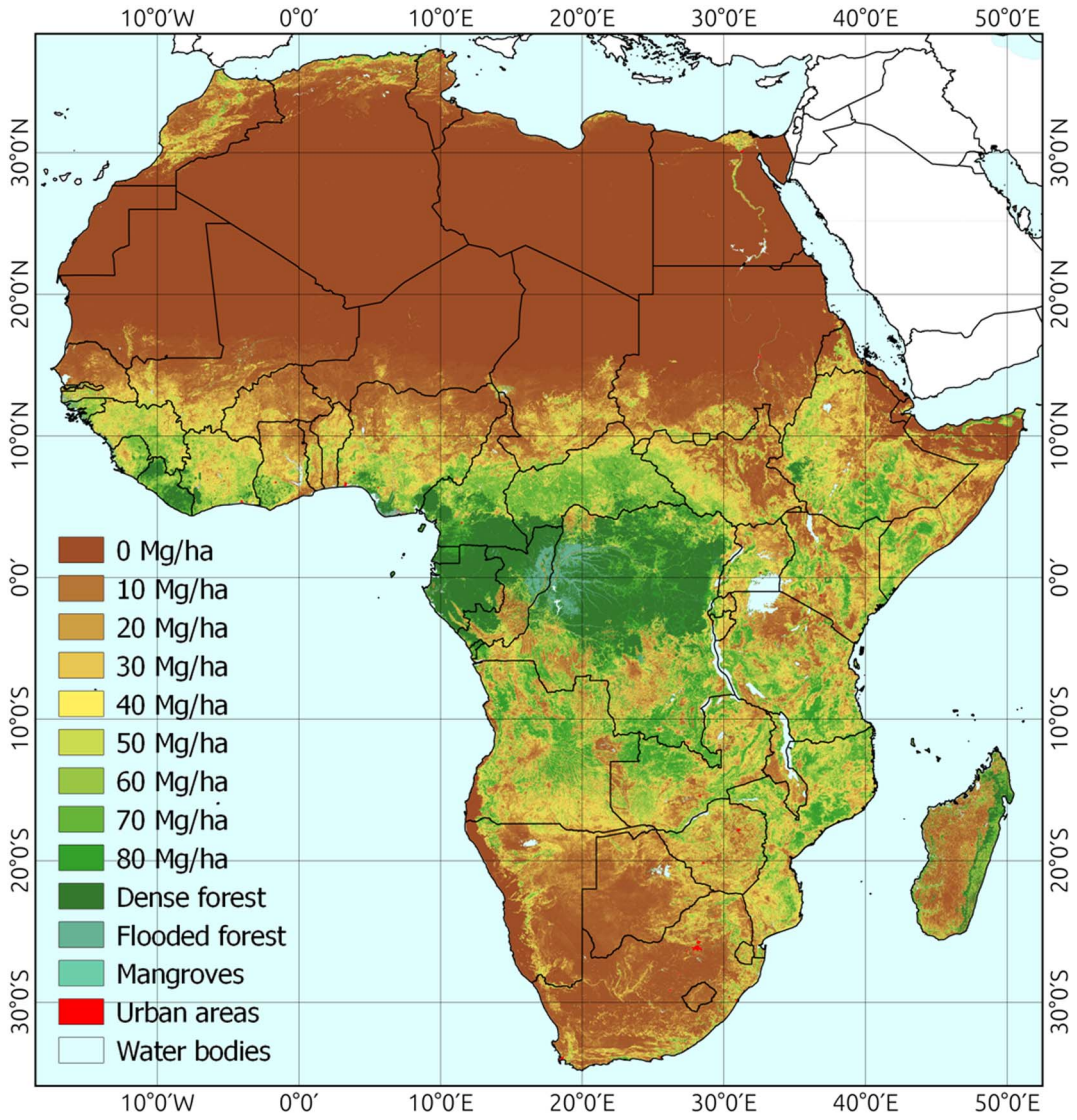

Fig. 6. The above-ground biomass map of African savannahs and woodlands at 25 m resolution derived in this study from the 2010 ALOS PALSAR mosaic.

and Baccini provide in this case incorrect estimates, around 30–40 Mg·ha^{-1}, probably because the spatial extrapolation of LiDAR samples with passive optical observations is misled by the grass layer. Besides, the two high resolution maps show fine details that cannot be seen in the three coarser resolution maps, like gallery forests along rivers.

The second cross-dataset comparison represents a “tiger bush” landscape in Sudan (Fig. 9), *i.e.* a patterned vegetation community consisting of alternating narrow bands of trees or shrubs, with bare ground or low herb cover in between, that run roughly parallel to contour lines of equal elevation in arid and semi-arid regions (Lefever and Lejeune, 1997). These patterns are too fine to be observed in the coarse resolution maps, but the 30 m resolution map by Baccini et al. (2015) also fails to capture these features, while they are clearly visible in the PALSAR map as well as in the very high resolution optical image shown in the figure. Our biomass estimates could therefore be helpful to understand the distribution and formation of tiger bush and other similar patterns occurring between savannah, forest and grassland on a wide scale, as a potential extension to what was done in small-scale studies using high-resolution optical imagery (Deblauwe et al., 2011).

Fig. 10 shows the precision and accuracy datasets calculated on a pixel basis as described in Section 4.7. The percent precision error represents $\sigma_{AGB\ est}/AGB_{est}$, where $\sigma_{AGB\ est}$ is the standard deviation of the AGB estimates obtained through repeated inversions affected by field and SAR measurement errors. In the savannahs and woodlands, this value is remarkably stable, at around 11% in the dry season areas and 14% in the wet season areas. The higher error values in the wet season areas reflect the smaller dynamic range of the backscatter-AGB relationships. In areas of very low/high AGB values (*i.e.* low/high HH and HV backscatters), the precision error falls to very low values as the AGB estimator consistently gives values close to the minimum/maximum invertible value. The 95% HPDI is represented by a map of its lower and higher bounds. The absolute accuracy error, approximated as the width of the 95% HPDI, *i.e.* the difference between the higher bound and the lower bound of the 95% HPDI, is found to be generally lower for low AGB areas and higher for high AGB areas. The relative accuracy error is however higher for low AGB areas, where it can reach values of 100%, for example in the case of a 10 Mg·ha^{-1} area with a 95% HPDI ranging from 0 to 20 Mg·ha^{-1}. It is worth noting that these accuracy figures are conservative estimates that represent the worst-case scenario corresponding to environmental conditions differing strongly from the average conditions considered in these “wet season” and “dry season” areas. In most cases, the actual errors are actually lower than the values suggested by the 95% HPDI.

The overall uncertainties, represented by the extended 95% HPDI, differ only very slightly from the accuracy error represented by the

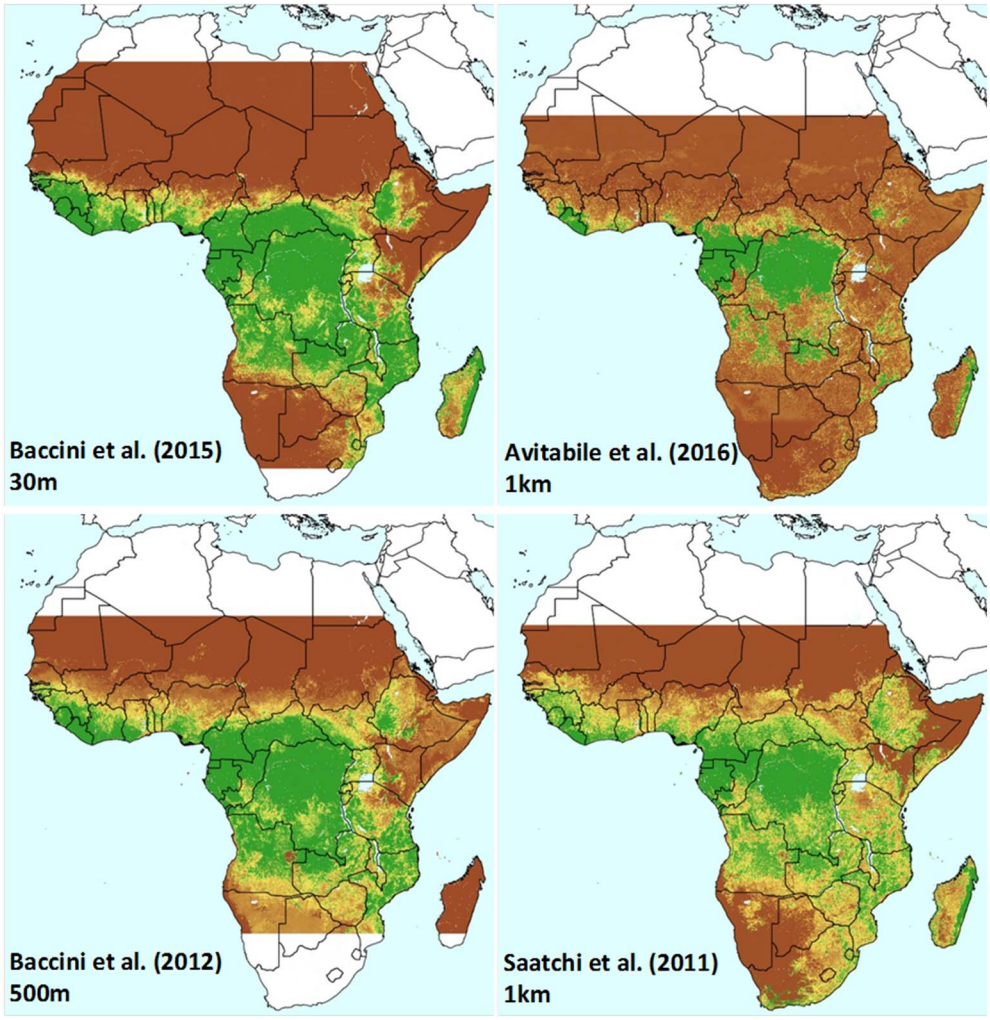

Fig. 7. The existing AGB maps in Africa, from Baccini et al. (2015) at 30 m, Avitabile et al. (2016) at 1 km, Baccini et al. (2012) at 500 m, and Saatchi et al. (2011) at 1 km.

regular 95% HPDI, and are therefore not represented here.

5.2. Validation

In order to validate the AGB dataset produced in this study, we used two different approaches. The first one is a cross-validation that uses the reference field dataset described in Section 3.1, and the second is a comparison with independent AGB estimates obtained from airborne LiDAR imagery in South Africa.

5.2.1. Monte-Carlo cross-validation

In this approach, we randomly split the reference dataset ($N = 144$) a thousand times into two equal subsets, one for training and one for validation, for the wet season area and the dry season area separatelyAt each iteration, the *a* and *c* parameters of the direct model are calibrated using the training dataset as described in Section 4.3, and the predictive accuracy of the Bayesian inversion is assessed using the validation data. Fig. 11 shows the distribution of the Root Mean Square Difference (RMSD) and correlation coefficient ρ of the corresponding 1000 AGB inversions. The overall mean RMSD, calculated at the plot scale, is 17.0 $Mg{\cdot}ha^{-1}$ (16.6 $Mg{\cdot}ha^{-1}$ for the wet season area and 17.1 $Mg{\cdot}ha^{-1}$ for the dry season areas) and the overall correlation coefficient is 0.76 (0.75 for the wet season area and 0.77 for the dry season areas). Note that these figures are calculated by keeping only *in situ* AGB estimates lower than 100 $Mg{\cdot}ha^{-1}$ in the analysis, because most field plots higher than 100 $Mg{\cdot}ha^{-1}$ are masked out during the post-processing, and they are overrepresented in our samples compared to the real distribution of AGB in the woodlands and savannahs of Africa. Including them in this cross-validation provides degraded results which are not thought to be representative of our dataset, which focuses on the 0–100 $Mg{\cdot}ha^{-1}$ biomass range: the overall mean RMSD reaches 46.3 Mg·ha-1 (wet season: 69.3 $Mg{\cdot}ha^{-1}$, dry season: 22.9 $Mg{\cdot}ha^{-1}$), and the overall correlation coefficient decreases to 0.60 (wet season: 0.61, dry season: 0.69).

5.2.2. LiDAR-based validation in South Africa

The second validation approach consisted in comparing the ALOS PALSAR AGB estimates with AGB estimates obtained from airborne LiDAR acquisitions over South African savannahs (Naidoo et al., 2015).

The LiDAR data was acquired by the Carnegie Airborne Observatory-2 AToMS sensor during April–May 2012 at a flight height of 1200 m with a scan frequency of 50 kHz, a laser spot spacing of 0.56 m, a point density of 6.4 points per m^2 and covered approximately 63,000 ha over the lowveld savannah region (Asner et al., 2012). A 1.1 m Digital Elevation Models (DEM) and top-of-canopy surface models (CSM) were created by processing the raw LiDAR point clouds according to the steps outlined in Asner et al. (2012). Canopy height models (CHM, pixel size of 1.12 m) were computed by subtracting the DEM from the CSM. The AGB LiDAR derived metric was modelled using a linear regression, ground estimated AGB (within 25 m field plots) and a simple H × CC LiDAR metric (where H is the mean top-of-canopy height and CC is the canopy cover of a 25 m pixel resolution) (Colgan et al., 2012). The RMSD of the LiDAR derived AGB estimates is reported to be 19.2 $Mg{\cdot}ha^{-1}$ (Naidoo et al., 2015).

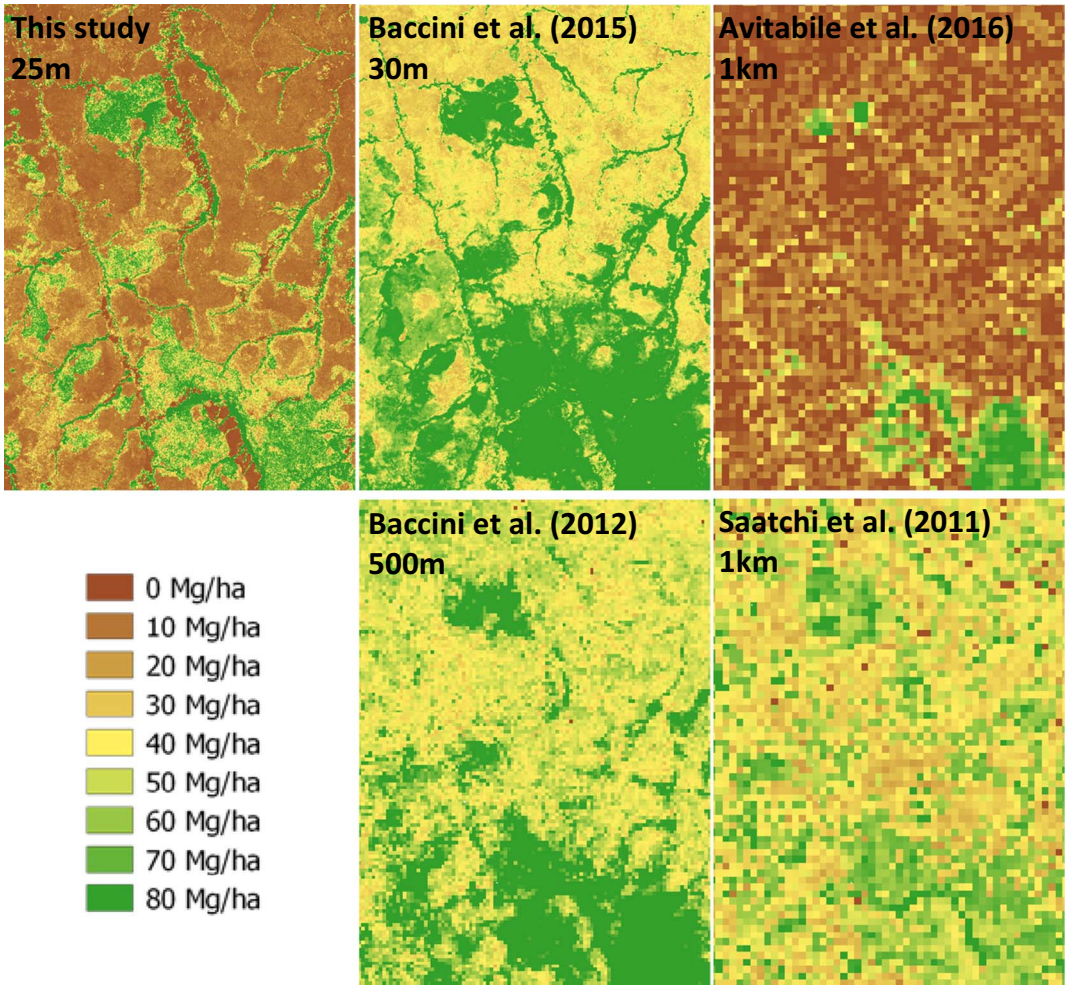

Fig. 8. Comparison between the AGB map produced in this study and the existing AGB maps in a subset located in the Democratic Republic of Congo, around geographic coordinates 6.4°S/18.4°E.

Fig. 12 shows a comparison between the AGB maps obtained from this LiDAR dataset and the corresponding AGB maps developed in this study from the PALSAR mosaics. The AGB patterns observed in the LiDAR data are remarkably well reproduced in the PALSAR maps and the range of AGB values in the two datasets are consistent.

We calculated the coefficient of determination ρ and RMSD between the AGB estimates from this LiDAR dataset on one hand, and the AGB estimates from the PALSAR data or from the 30 m resolution dataset of Baccini et al. (2015) on the other hand. The PALSAR dataset produced in this study generally performs better than the 30 m Baccini dataset over these savannah and woodland landscapes, with a ρ of 0.84 (0.58 for Baccini) and RMSD of 7.7 $Mg{\cdot}ha^{-1}$ (10.8 $Mg{\cdot}ha^{-1}$ for Baccini), despite a slight overestimation for AGB values larger than 40 $Mg{\cdot}ha^{-1}$. The corresponding scatterplots are shown in Fig. 13, and reveal that unlike our estimates, the estimates from Baccini et al. (2015) are significantly biased with respect to the LiDAR estimates. Note that the outstanding agreement between our dataset and the LiDAR dataset, although covering a variety of soil types (granitic, basaltic) and land management practices (communal rangelands, protected areas), is limited to a small region of a specific biome (the lowveld) and may not be representative of the whole African savannahs.

5.3. Analysis of carbon stocks in African countries

The AGB dataset produced in this study was used to assess the above-ground biomass and carbon contained in all African countries, except the small insular countries (Cape Verde, Comoros, Mauritius, São Tomé and Príncipe, and Seychelles). To account for the limitations of the method, which estimates AGB only until 85 $Mg{\cdot}ha^{-1}$, we assigned to the masked dense forest and flooded forest pixels an AGB of 300 $Mg{\cdot}ha^{-1}$. This value was chosen as a trade-off between the AGB estimates of tropical forest reported in Saugier et al. (2001) (390 Mg·ha − 1) and in FAO (2001) (190 $Mg{\cdot}ha^{-1}$), and of African equatorial forest reported in IPCC (2006) (400 $Mg{\cdot}ha^{-1}$) and Gibbs and Brown (2007) (198 $Mg{\cdot}ha^{-1}$). Mangroves were assigned an AGB value calculated in each country from the Saatchi et al. (2011) estimates. The total AGB of each country is calculated from the ALOS PALSAR AGB dataset, and transformed to above-ground carbon stocks by using a 0.5 conversion factor. The C stocks per country (broken down into dense forests, savannahs and woodlands, and total) are reported in Table S2, together with the proportion of the country area masked as dense forests, flooded forests, mangroves, urban areas, and water bodies.

Fig. 14 shows a comparison between the national carbon stocks estimated in this study and those estimated by FAO, Saatchi et al. (2011), Baccini et al. (2012) and Avitabile et al. (2016). The corresponding values are also reported in Table S2. Our carbon stocks estimates are generally very well correlated with the other remote-sensing-based estimates (correlation coefficient ρ between 0.94 and 0.97). The correlation with the estimates from FAO is slightly lower (ρ = 0.84), but the same is true when the other remote-sensing-based estimates are compared with FAO (ρ = 0.87 to 0.90, see Fig. S1). Our estimates provide slightly higher total carbon stocks compared to FAO (+ 6.8%). This could be partly explained by the fact that we account for the total AGB of each country while FAO estimates the carbon stocks of forests

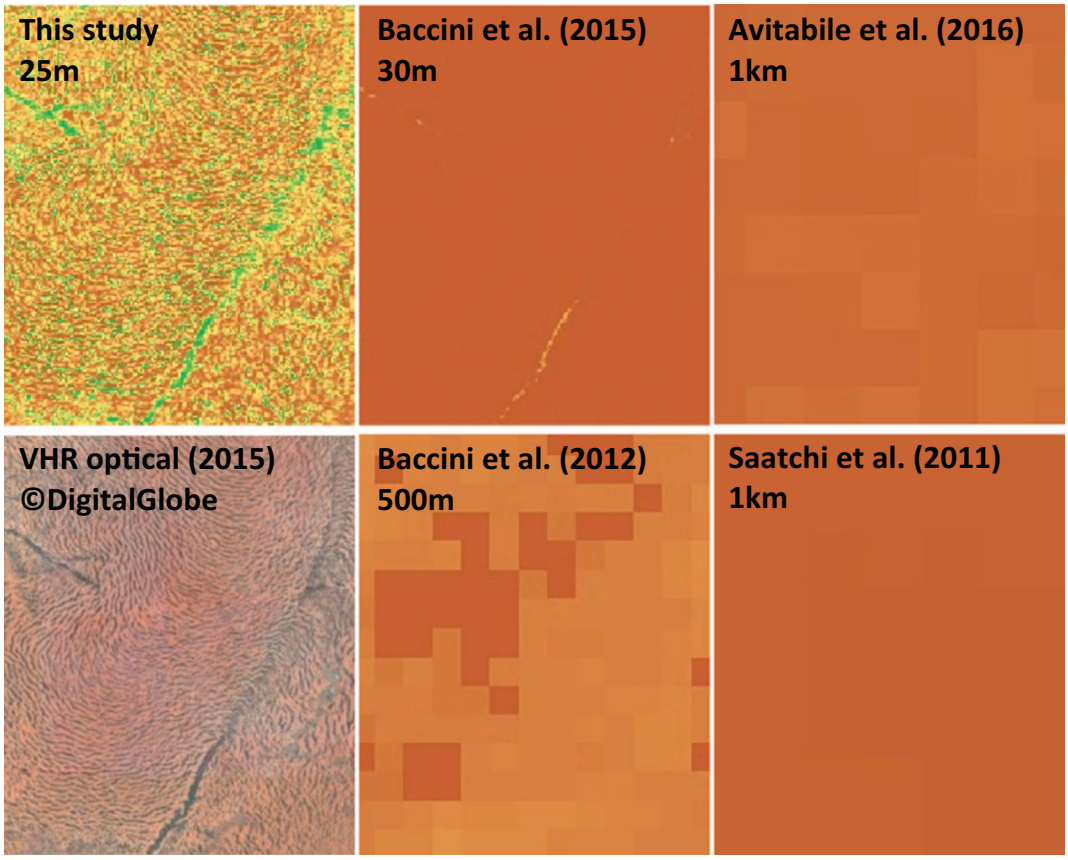

Fig. 9. Comparison between the AGB map produced in this study and the existing AGB maps in a "tiger bush" region located in Sudan, around geographic coordinates 11.26°N/28.23°E. The legend is the same as in Fig. 8. The bottom left panel represents a VHR optical image visualized in Google Earth.

only, which are defined as vegetation patches with a minimum tree cover of 10% and minimum area of 0.5 ha. The comparison between our estimates and the FAO estimates can therefore give an idea of the amount of carbon that is ignored when only forests are considered. It can also be noted that the FAO estimates are based on reports provided by each country, and some countries have limited capacities to estimate their carbon stocks accurately. Our total estimates are very similar to those of Saatchi et al. (2011) (−1.5%), while we provide significantly lower values than Baccini et al. (2012) (−11.8%), and higher values than Avitabile et al. (2016) (+19.4%). These discrepancies can be further analysed by considering the calculated carbon stock density in each country (in $MtC{\cdot}ha^{-1}$). Fig. S2 reveals that our dataset tends to provide lower AGB estimates than Baccini et al. (2012) in countries dominated by savannahs and woodlands and higher AGB estimates in the countries dominated by dense forests, while the opposite is true with Avitabile et al. (2016). The comparison between the mean national carbon stock densities calculated in our study and in Saatchi et al. (2011) show highly-correlated and almost unbiased estimates.

The values calculated in this study show that 52% of the total African above-ground carbon is stored in savannahs and woodlands, and 48% in dense forests (including mangroves and flooded forests).

5.4. Caveats

While the validation approaches adopted in Section 5.2 indicate that the AGB dataset described in this paper has a good accuracy (RMSD of 17 $Mg{\cdot}ha^{-1}$ for the cross-validation with the field plots from all Africa, and 7.7 $Mg{\cdot}ha^{-1}$ for the local validation in the South African lowveld), it is still worth mentioning a few caveats linked to the intrinsic limitations of the PALSAR mosaic dataset and of the method.

First, as already mentioned in Section 4.1, our approach consists in estimating AGB separately in the "wet season areas" and in the "dry season areas" in order to minimize the backscatter variation linked to non-homogeneous environmental conditions (soil moisture levels or vegetation phenology). However, these environmental conditions can locally deviate significantly from the average environmental conditions of the area they belong to (wet season area or dry season area), for example in case of a heavy rainfall shortly before the PALSAR acquisition in the dry season area or an exceptional draught in the wet season area. In such cases, the AGB estimates will be locally affected by substantial errors. These errors are nonetheless taken into account in the calculation of the 95% HPDI.

Another source of error is the influence of topography, which affects the backscatter in two ways: it changes the pixel scattering area, and it modifies the local incidence angle and therefore the response of the target. Although both these impacts have been reduced in the production of the PALSAR mosaics (Shimada and Ohtaki, 2010), it is not possible to correct them perfectly and residual topographic distortions remain. As a consequence, the AGB estimates are less reliable in areas of strong topography.

Masking out land cover classes where the AGB is not estimated (dense forests, flooded forests, mangroves, urban areas, water bodies, and bare areas embedded with rocks), as described in Section 4.6, can also locally degrade the information content of our dataset. Because the land cover datasets used for masking have a coarser resolution and have their own errors, of, these areas are imperfectly masked out. In particular in forest/savannah transition areas, it is expected that small dense forest pockets and gallery forests will not be masked out and will be assigned an AGB value lower than their actual value, while small savannah pockets inside dense forest areas will be masked out.

The national estimates provided in Section 5.3 can therefore be affected by the quality of the masking, and by other assumptions used

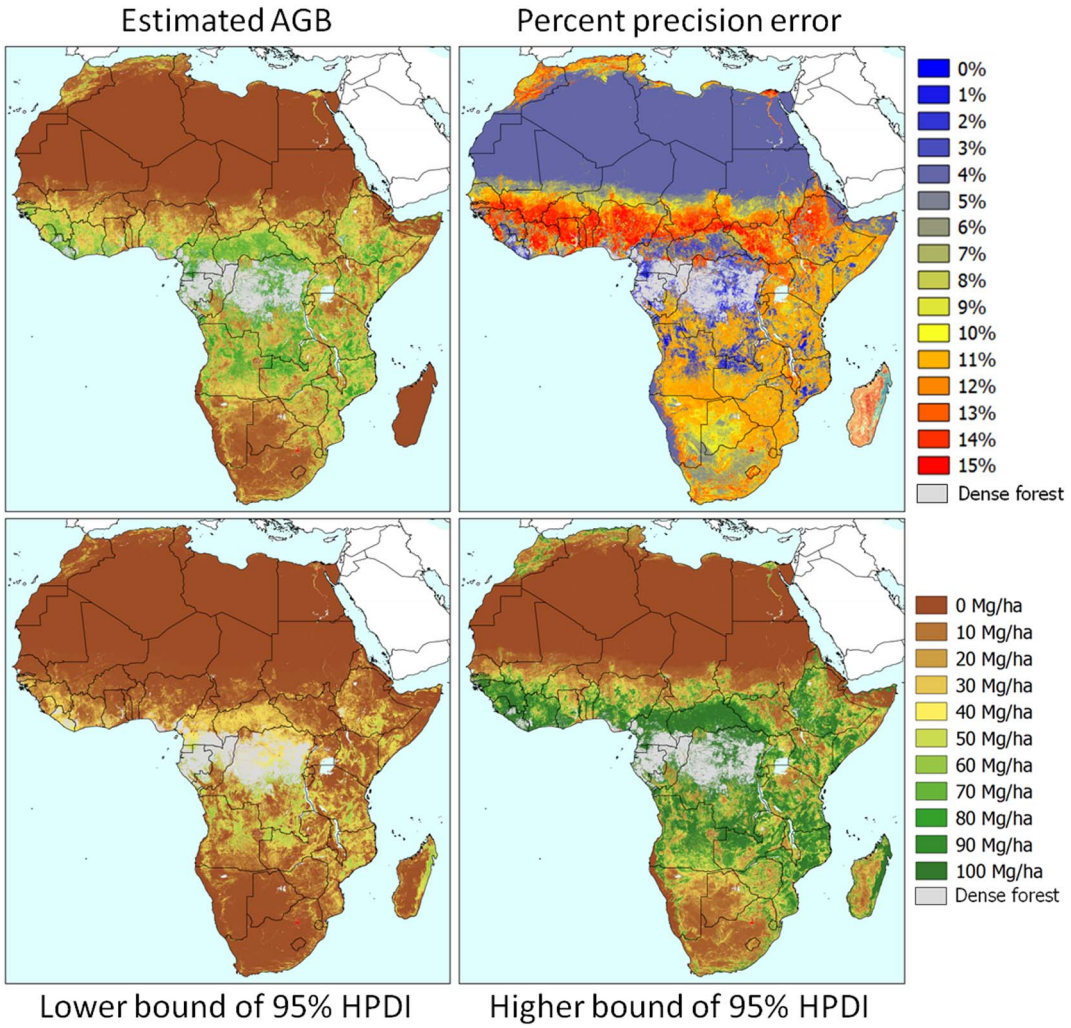

Fig. 10. The AGB dataset produced in this study, together with the percent precision error and with the minimum and maximum values of the HPDI. Dense forests (including flooded forests and mangroves) are masked in grey.

in the calculation (*e.g.* the assignment of an AGB equal to 300 Mg·ha^{-1} for the dense forests). The overall accuracy of the retained/not-retained classification used for masking (where the "not-retained" class contains all the CCI Land Cover classes for which we do not want to provide AGB estimates, *i.e.* dense forest biomes and non-vegetated areas) has been calculated to be equal to 95% from the confusion matrix provided in the Land Cover CCI Product User Guide. Therefore, the quality of the masking should not affect national estimates to a large extent. Regarding the AGB values assigned to "dense forests", we have re-calculated the total carbon stocks per country using AGB values from Saatchi et al. for the dense forests, instead of the 300 Mg·ha^{-1} default value, and the results are very similar (ρ = 1.0, RMSD = 5.05 Mg·ha^{-1} for the mean national carbon density).

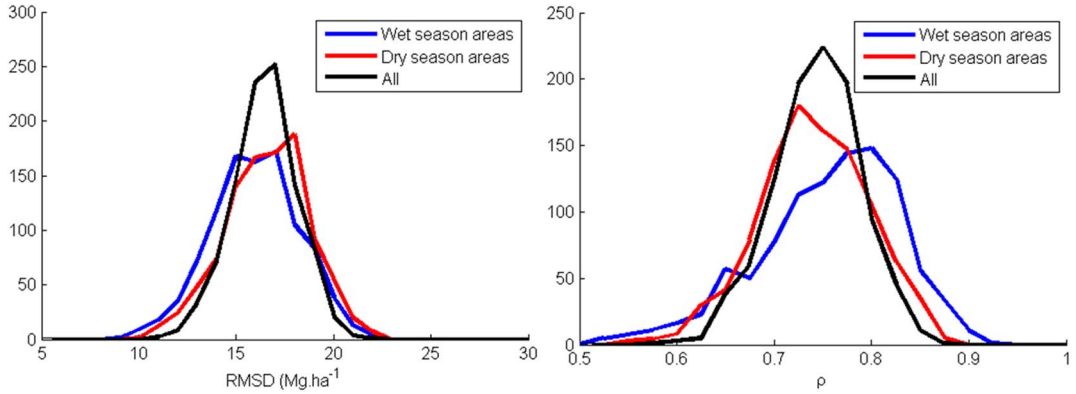

Fig. 11. Distribution of the RMSD and correlation coefficient ρ over the 1000 simulations of the cross-validation. At each simulation, the reference dataset is randomly split into two equal subsets, one for training and one for validation, keeping only *in situ* AGB estimates lower than 100 Mg·ha^{-1}.

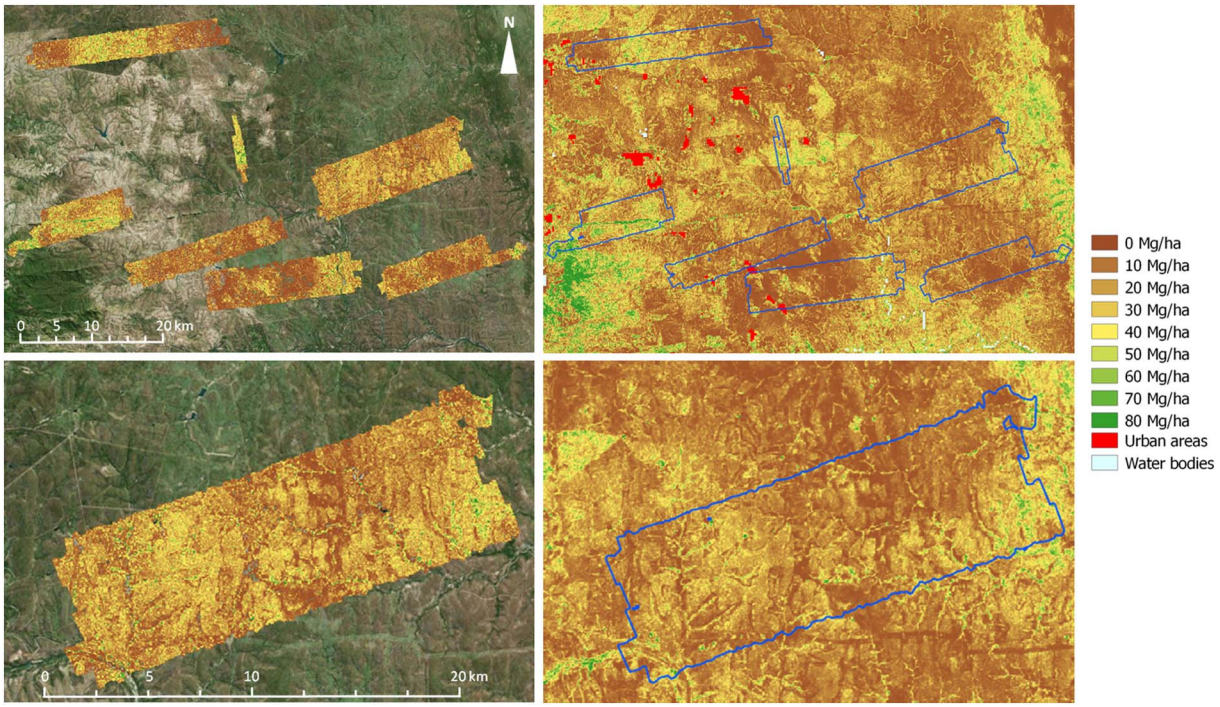

Fig. 12. Comparison between AGB estimated over the LiDAR dataset (left) and from the PALSAR mosaic (right) over the whole LiDAR dataset (top) and over a close-up of one of the LiDAR patches (bottom).

6. Conclusion

Based on a dual-polarisation PALSAR mosaic produced from ALOS PALSAR imagery acquired in 2010, we developed the first 25 m resolution wall-to-wall map of Africa dedicated specifically to the AGB of savannahs and woodlands, a biome of paramount importance in the carbon budget of this continent.

Visual comparisons of our AGB dataset with the other AGB datasets at similar (30 m) or coarser (300 m to 1 km) resolutions, and with independent estimates from an airborne LiDAR dataset in a savannah area, highlight the merits of our dataset in the savannahs and woodlands areas, both in terms of resolution and sensitivity. Uncertainties linked in particular to the effects of the environmental conditions are minimised by performing the AGB inversion in “dry season” and “wet season” areas separately. Errors associated with remaining environmental effects are estimated and provided at the pixel level in the form of a credible interval, the 95% HPDI, which reveals potentially large errors locally when the environmental conditions contrast drastically with the average conditions of each area. Two validation approaches, namely one cross-validation with the *in situ* dataset and a validation with a LiDAR AGB dataset, reveal a good accuracy of our dataset, with an RMSD between 8 and 17 $Mg{\cdot}ha^{-1}$. Finally, the dataset has been used to provide estimates of the total national carbon stocks of most African countries, which have been compared to other estimates from FAO and existing AGB maps.

The approach developed in this study can be applied to similar L-band mosaics produced at later epochs, for example the ALOS-2 PALSAR-2 mosaics that are being produced on a yearly basis since 2015, or on the open forests of other continents. To do so, the model developed in Africa in 2010 in this study would require minor

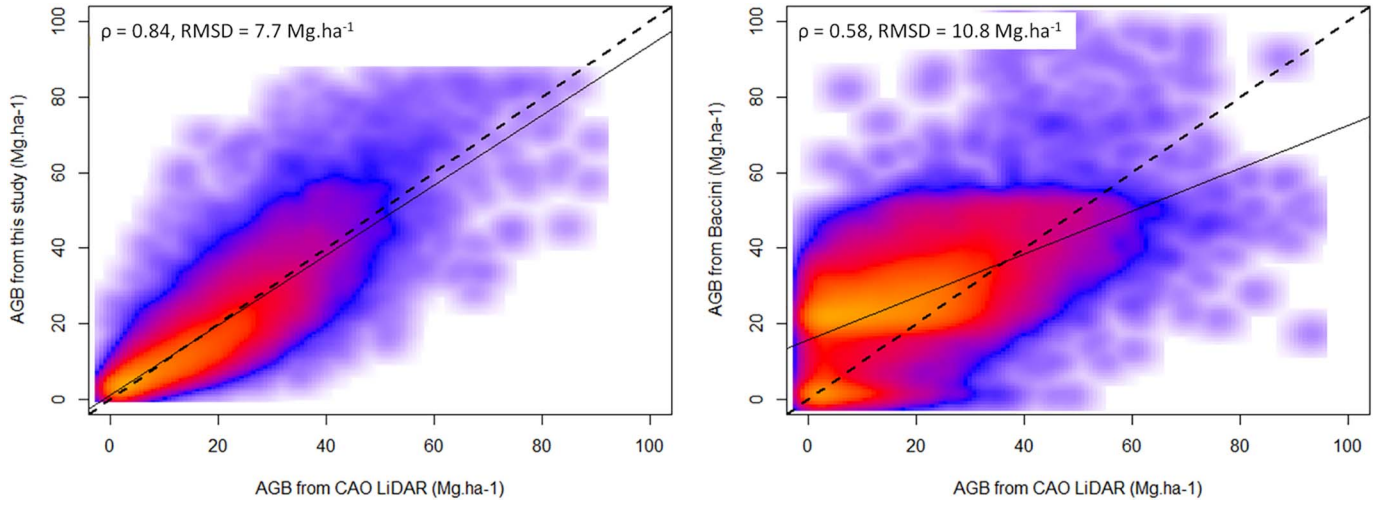

Fig. 13. Scatterplots between the CAO LiDAR AGB estimates and the AGB estimates from this study (left) or from the AGB estimates at 30 m by Baccini et al. (2015). The dashed line is the 1:1 line and the plain line represents the linear regression.

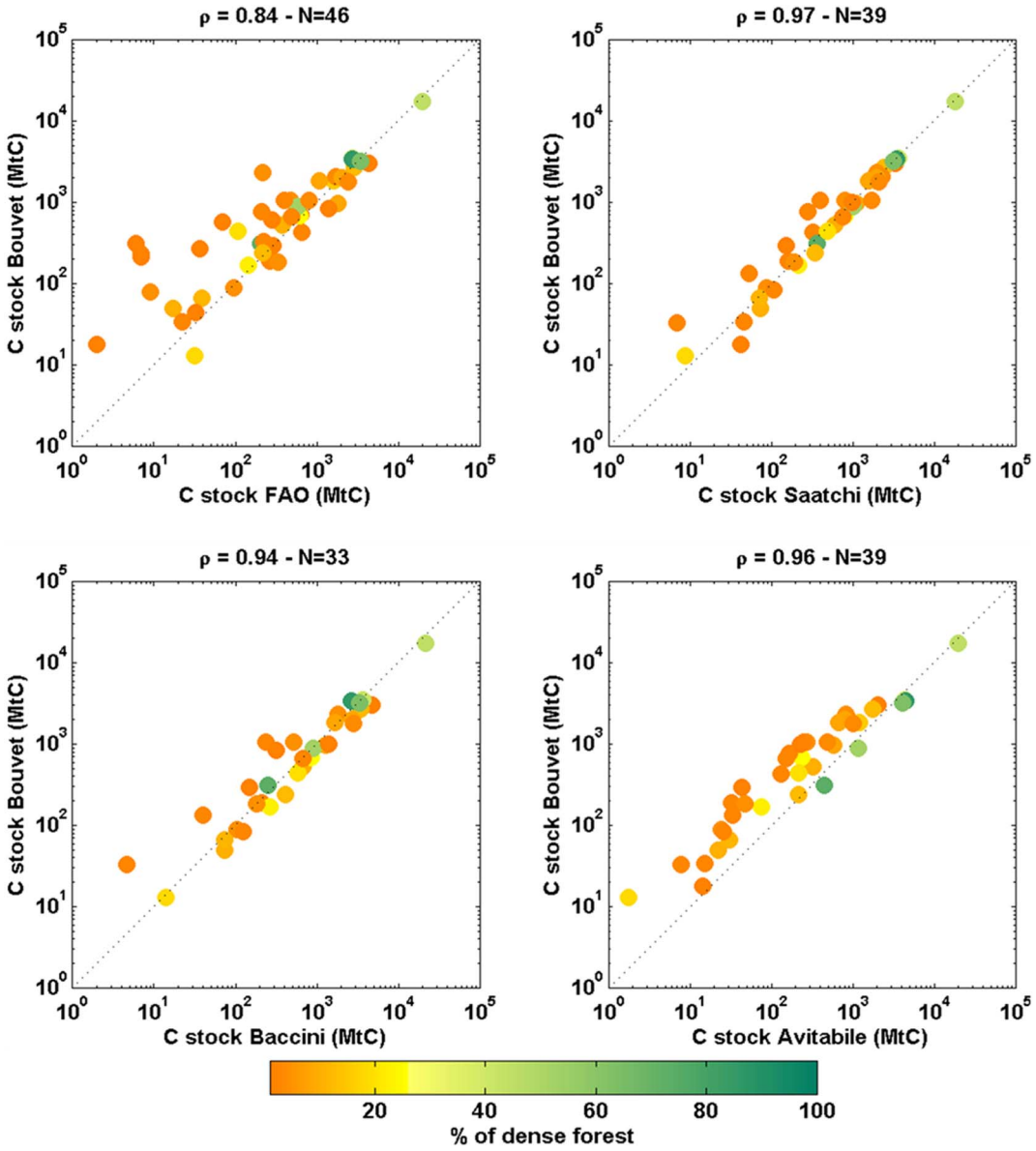

Fig. 14. Comparison between the national above-ground carbon stocks estimated from the AGB map produced in this study and the carbon stocks reported by FAO (top left), in Saatchi et al. (2011) (top right), in Baccini et al. (2012) (bottom left) and in Avitabile et al. (2016) (bottom right). Each dot represents one country, and their color represents the percentage of dense forests in the country. N is the number of countries common to each pair of data.

adjustments to account for systematic radiometric differences occurring in the production of the mosaics. In the case of other continents, these adjustments would ideally require another set of high quality *in situ* AGB estimates. In the absence of such high quality *in situ* datasets, other approaches that do not rely on *in situ* measurements, as described in previous studies over temperate or boreal forests (Cartus et al., 2012), can be considered. The potential of such methods in tropical woodlands and savannahs should therefore be investigated, *e.g.* in comparison with the results produced in this study. In the future, the L-band time-series that will be provided by NISAR will provide a good opportunity to correct for errors linked to local variations of the environmental conditions, and therefore to overcome the major limitation of our approach based on mono-temporal mosaic datasets only.

Acknowledgements

The authors would like to thank Edward Mitchard from University of Edinburgh for providing some *in situ* data and Masanobu Shimada and his team from JAXA for providing the global 25 m resolution PALSAR Mosaics. This data is owned by JAXA.

The CCI Land Cover (CCI-LC) database has been processed by the CCI-LC consortium led by UCL-Geomatics (Belgium), and is made available to the public by ESA and the consortium. © ESA Climate Change Initiative - Land Cover project 2014.

The authors gratefully acknowledge financial support from CNES (TOSCA program, purchase order BCT_71SC), from ESA (DUE GlobBiomass project, ESA Contract No. 4000113100/14/I-NB) and from the European Union's Horizon 2020 Research and Innovation Programme under grant agreement No. 685761 (EOMonDis project).

Appendix A. Supplementary data

Supplementary data to this article can be found online at https://doi.org/10.1016/j.rse.2017.12.030.

References

Achard, F., Eva, H.D., Stibig, H.-J., Mayaux, P., Gallego, J., Richards, T., Malingreau, J.-P., 2002. Determination of deforestation rates of the world's humid tropical forests. Science 297, 999–1002. http://dx.doi.org/10.1126/science.1070656.

Achard, F., Eva, H.D., Mayaux, P., Stibig, H.-J., Belward, A., 2004. Improved estimates of net carbon emissions from land cover change in the tropics for the 1990s. Glob. Biogeochem. Cycles 18 GB2008. https://doi.org/10.1029/2003GB002142.

Arino, Olivier, Perez, Ramos, Julio, Jose, Kalogirou, Vasileios, Bontemps, Sophie, Defourny, Pierre, Van Bogaert, Eric, 2012. Global Land Cover Map for 2009 (GlobCover 2009).

Asner, G.P., Knapp, D.E., Boardman, J., Green, R.O., Kennedy-Bowdoin, T., Eastwood, M., Martin, R.E., Anderson, C., Field, C.B., 2012. Carnegie airborne observatory-2: increasing science data dimensionality via high-fidelity multi-sensor fusion. Remote Sens. Environ. 124, 454–465. http://dx.doi.org/10.1016/j.rse.2012.06.012.

Attema, E.P.W., Ulaby, F.T., 1978. Vegetation modeled as a water cloud. Radio Sci. 13, 357–364. http://dx.doi.org/10.1029/RS013i002p00357.

Avitabile, V., Herold, M., Heuvelink, G.B.M., Lewis, S.L., Phillips, O.L., Asner, G.P., Armston, J., Ashton, P.S., Banin, L., Bayol, N., Berry, N.J., Boeckx, P., de Jong, B.H.J., DeVries, B., Girardin, C.A.J., Kearsley, E., Lindsell, J.A., Lopez-Gonzalez, G., Lucas, R., Malhi, Y., Morel, A., Mitchard, E.T.A., Nagy, L., Qie, L., Quinones, M.J., Ryan, C.M., Ferry, S.J.W., Sunderland, T., Laurin, G.V., Gatti, R.C., Valentini, R., Verbeeck, H., Wijaya, A., Willcock, S., 2016. An integrated pan-tropical biomass map using multiple reference datasets. Glob. Chang. Biol. 22, 1406–1420. http://dx.doi.org/10.1111/gcb.13139.

Baccini, A., Goetz, S.J., Walker, W.S., Laporte, N.T., Sun, M., Sulla-Menashe, D., Hackler, J., Beck, P.S.A., Dubayah, R., Friedl, M.A., Samanta, S., Houghton, R.A., 2012. Estimated carbon dioxide emissions from tropical deforestation improved by carbon-density maps. Nat. Clim. Chang. 2, 182–185. http://dx.doi.org/10.1038/nclimate1354.

Baccini, A., Walker, W., Carvalho, L., Farina, M., Sulla-Menashe, D., Houghton, R.A., 2015. Tropical forests are a net carbon source based on new measurements of gain and loss. In: In review. Accessed through Global Forest Watch Climate on 2016/07/25, . climate.globalforestwatch.org.

Bartholomé, E., Belward, A.S., 2005. GLC2000: a new approach to global land cover mapping from earth observation data. Int. J. Remote Sens. 26, 1959–1977. http://dx.doi.org/10.1080/01431160412331291297.

Bastin, J.-F., Berrahmouni, N., Grainger, A., Maniatis, D., Mollicone, D., Moore, R., Patriarca, C., Picard, N., Sparrow, B., Abraham, E.M., Aloui, K., Atesoglu, A., Attore, F., Bassüllü, Ç., Bey, A., Garzuglia, M., García-Montero, L.G., Groot, N., Guerin, G., Laestadius, L., Lowe, A.J., Mamane, B., Marchi, G., Patterson, P., Rezende, M., Ricci, S., Salcedo, I., Diaz, A.S.-P., Stolle, F., Surappaeva, V., Castro, R., 2017. The extent of forest in dryland biomes. Science 356, 635–638. http://dx.doi.org/10.1126/science.aam6527.

Bodart, C., Brink, A.B., Donnay, F., Lupi, A., Mayaux, P., Achard, F., 2013. Continental estimates of forest cover and forest cover changes in the dry ecosystems of Africa between 1990 and 2000. J. Biogeogr. 40, 1036–1047. http://dx.doi.org/10.1111/jbi.12084.

Bombelli, A., Henry, M., Castaldi, S., Adu-Bredu, S., Arneth, A., de Grandcourt, A., Grieco, E., Kutsch, W.L., Lehsten, V., Rasile, A., Reichstein, M., Tansey, K., Weber, U., Valentini, R., 2009. An outlook on the Sub-Saharan Africa carbon balance. Biogeosciences 6, 2193–2205. http://dx.doi.org/10.5194/bg-6-2193-2009.

Bond, W.J., Midgley, G.F., 2012. Carbon dioxide and the uneasy interactions of trees and savannah grasses. Philos. Trans. R. Soc. B 367, 601–612. http://dx.doi.org/10.1098/rstb.2011.0182.

Brink, A.B., Eva, H.D., 2009. Monitoring 25 years of land cover change dynamics in Africa: a sample based remote sensing approach. Appl. Geogr. 29, 501–512. http://dx.doi.org/10.1016/j.apgeog.2008.10.004.

Bruniquel, J., Lopes, A., 1997. Multi-variate optimal speckle reduction in SAR imagery. Int. J. Remote Sens. 18, 603–627. http://dx.doi.org/10.1080/014311697218962.

Carreiras, J.M.B., Vasconcelos, M.J., Lucas, R.M., 2012. Understanding the relationship between aboveground biomass and ALOS PALSAR data in the forests of Guinea-Bissau (West Africa). Remote Sens. Environ. 121, 426–442. http://dx.doi.org/10.1016/j.rse.2012.02.012.

Carreiras, J.M.B., Melo, J.B., Vasconcelos, M.J., 2013. Estimating the above-ground biomass in Miombo savanna woodlands (Mozambique, East Africa) using L-band synthetic aperture radar data. Remote Sens. 5, 1524–1548. http://dx.doi.org/10.3390/rs5041524.

Cartus, O., Santoro, M., Kellndorfer, J., 2012. Mapping forest aboveground biomass in the northeastern United States with ALOS PALSAR dual-polarization L-band. Remote Sens. Environ. 124, 466–478. http://dx.doi.org/10.1016/j.rse.2012.05.029.

Cartus, O., Kellndorfer, J., Walker, W., Franco, C., Bishop, J., Santos, L., Fuentes, J.M.M., 2014. A national, detailed map of forest aboveground carbon stocks in Mexico. Remote Sens. 6, 5559–5588. http://dx.doi.org/10.3390/rs6065559.

Castel, T., Beaudoin, A., Stach, N., Stussi, N., Toan, T.L., Durand, P., 2001. Sensitivity of space-borne SAR data to forest parameters over sloping terrain. Theory and experiment. Int. J. Remote Sens. 22, 2351–2376. http://dx.doi.org/10.1080/01431160121407.

Chave, J., Condit, R., Aguilar, S., Hernandez, A., Lao, S., Perez, R., 2004. Error propagation and scaling for tropical forest biomass estimates. Philos. Trans. R. Soc., B 359, 409–420. http://dx.doi.org/10.1098/rstb.2003.1425.

Chave, J., Andalo, C., Brown, S., Cairns, M.A., Chambers, J.Q., Eamus, D., Fölster, H., Fromard, F., Higuchi, N., Kira, T., Lescure, J.-P., Nelson, B.W., Ogawa, H., Puig, H., Riéra, B., Yamakura, T., 2005. Tree allometry and improved estimation of carbon stocks and balance in tropical forests. Oecologia 145, 87–99. http://dx.doi.org/10.1007/s00442-005-0100-x.

Chidumayo, E.N., Gumbo, D.J. (Eds.), 2010. The Dry Forests and Woodlands of Africa: Managing for Products and Services. Earthscan, London, UK.

Ciais, P., Piao, S.-L., Cadule, P., Friedlingstein, P., Chédin, A., 2009. Variability and recent trends in the African terrestrial carbon balance. Biogeosciences 6, 1935–1948. http://dx.doi.org/10.5194/bg-6-1935-2009.

Ciais, P., Bombelli, A., Williams, M., Piao, S.L., Chave, J., Ryan, C.M., Henry, M., Brender, P., Valentini, R., 2011. The carbon balance of Africa: synthesis of recent research studies. Philos. Trans. R. Soc. Lond. A Math. Phys. Eng. Sci. 369, 2038–2057. http://dx.doi.org/10.1098/rsta.2010.0328.

Colgan, M.S., Asner, G.P., Levick, S.R., Martin, R.E., Chadwick, O.A., 2012. Topo-edaphic controls over woody plant biomass in south African savannas. Biogeosciences 9, 1809–1821. http://dx.doi.org/10.5194/bg-9-1809-2012.

Deblauwe, V., Couteron, P., Lejeune, O., Bogaert, J., Barbier, N., 2011. Environmental modulation of self-organized periodic vegetation patterns in Sudan. Ecography 34, 990–1001. http://dx.doi.org/10.1111/j.1600-0587.2010.06694.x.

DeFries, R.S., Houghton, R.A., Hansen, M.C., Field, C.B., Skole, D., Townshend, J., 2002. Carbon emissions from tropical deforestation and regrowth based on satellite observations for the 1980s and 1990s. PNAS 99, 14256–14261. http://dx.doi.org/10.1073/pnas.182560099.

Eldridge, D.J., Bowker, M.A., Maestre, F.T., Roger, E., Reynolds, J.F., Whitford, W.G., 2011. Impacts of shrub encroachment on ecosystem structure and functioning: towards a global synthesis. Ecol. Lett. 14, 709–722. http://dx.doi.org/10.1111/j.1461-0248.2011.01630.x.

Engelman, R., 2016. Africa's Population Will Soar Dangerously Unless Women Are More Empowered [WWW Document]. Scientific American URL. http://www.scientificamerican.com/article/africa-s-population-will-soar-dangerously-unless-women-are-more-empowered/, Accessed date: 1 August 2016.

Fearnside, P.M., 2000. Global warming and tropical land-use change: greenhouse gas emissions from biomass burning, decomposition and soils in forest conversion, shifting cultivation and secondary vegetation. Clim. Chang. 46, 115–158. http://dx.doi.org/10.1023/A:1005569915357.

Food and Agriculture Organization of the United Nations, 2001. Global forest resources assessment 2000.

Gibbs, H.K., Brown, S., 2007. Geographical Distribution of Woody Biomass Carbon in Tropical Africa: An Updated Database for 2000.

Haeusler, T., Gomez, S., Siwe, R., Le Toan, T., Mermoz, S., Schardt, M., Schmitt, U., Sannier, C., 2012. Reducing emissions from deforestation and degradation in Africa (REDDAF). In: Let's Embrace Space, Volume II - Space Research Achievements under the 7th Framework Programme. EU Publications.

Harrell, P.A., Kasischke, E.S., Bourgeau-Chavez, L.L., Haney, E.M., Christensen, N.L., 1997. Evaluation of approaches to estimating aboveground biomass in Southern pine forests using SIR-C data. In: Remote Sensing of Environment, Spaceborne Imaging Radar Mission. 59. pp. 223–233. http://dx.doi.org/10.1016/S0034-4257(96)00155-1.

Hijmans, R.J., Cameron, S.E., Parra, J.L., Jones, P.G., Jarvis, A., 2005. Very high resolution interpolated climate surfaces for global land areas. Int. J. Climatol. 25, 1965–1978. http://dx.doi.org/10.1002/joc.1276.

Hirota, M., Holmgren, M., Nes, E.H.V., Scheffer, M., 2011. Global resilience of tropical forest and savanna to critical transitions. Science 334, 232–235. http://dx.doi.org/10.1126/science.1210657.

Houghton, R.A., Hackler, J.L., 2006. Emissions of carbon from land use change in sub-Saharan Africa. J. Geophys. Res. 111, G02003. http://dx.doi.org/10.1029/2005JG000076.

Houghton, R.A., Hall, F., Goetz, S.J., 2009. Importance of biomass in the global carbon cycle. J. Geophys. Res. 114 G00E03. https://doi.org/10.1029/2009JG000935.

Imhoff, M., 1995. Theoretical analysis of the effect of forest structure on synthetic aperture radar backscatter and the remote sensing of biomass. IEEE Trans. Geosci. Remote Sens. 33, 341–352. http://dx.doi.org/10.1109/36.377934.

IPCC, 2006. In: National Greenhouse Gas Inventories Programme, Eggleston, H.S., Buendia, L., Miwa, K., Ngara, T., Tanabe, K. (Eds.), 2006 IPCC Guidelines for National Greenhouse Gas Inventories. IGES, Japan.

Kasischke, E.S., Tanase, M.A., Bourgeau-Chavez, L.L., Borr, M., 2011. Soil moisture limitations on monitoring boreal forest regrowth using spaceborne L-band SAR data. Remote Sens. Environ. 115, 227–232. http://dx.doi.org/10.1016/j.rse.2010.08.022.

Köppen, W., 1936. Das geographische System der Klimate. In: Handbuch der Klimatologie. Borntraeger.

Le Toan, T., Beaudoin, A., Riom, J., Guyon, D., 1992. Relating forest biomass to SAR data. IEEE Trans. Geosci. Remote Sens. 30, 403–411. http://dx.doi.org/10.1109/36.134089.

Le Toan, T., Quegan, S., Davidson, M.W.J., Balzter, H., Paillou, P., Papathanassiou, K., Plummer, S., Rocca, F., Saatchi, S., Shugart, H., Ulander, L., 2011. The BIOMASS mission: mapping global forest biomass to better understand the terrestrial carbon cycle. In: Remote Sensing of Environment, DESDynI VEG-3D Special Issue. 115. pp. 2850–2860. http://dx.doi.org/10.1016/j.rse.2011.03.020.

Lefever, R., Lejeune, O., 1997. On the origin of tiger bush. Bull. Math. Biol. 59, 263–294. http://dx.doi.org/10.1016/S0092-8240(96)00072-9.

Lefsky, M.A., Harding, D.J., Keller, M., Cohen, W.B., Carabajal, C.C., Del Bom Espirito-Santo, F., Hunter, M.O., de Oliveira, R., 2005. Estimates of forest canopy height and aboveground biomass using ICESat. Geophys. Res. Lett. 32 L22S02. https://doi.org/10.1029/2005GL023971.

Lucas, R., Armston, J., Fairfax, R., Fensham, R., Accad, A., Carreiras, J., Kelley, J., Bunting, P., Clewley, D., Bray, S., Metcalfe, D., Dwyer, J., Bowen, M., Eyre, T., Laidlaw, M., Shimada, M., 2010. An evaluation of the ALOS PALSAR L-band backscatter—above ground biomass relationship Queensland, Australia: impacts of surface moisture condition and vegetation structure. IEEE J. Sel. Top. Appl. Earth

Observ. Rem. Sens. 3, 576–593. http://dx.doi.org/10.1109/JSTARS.2010.2086436.
Massonnet, D., Souyris, J.-C., 2008. Imaging with Synthetic Aperture Radar. CRC Press.
Mathieu, R., Naidoo, L., Cho, M.A., Leblon, B., Main, R., Wessels, K., Asner, G.P., Buckley, J., Van Aardt, J., Erasmus, B.F.N., Smit, I.P.J., 2013. Toward structural assessment of semi-arid African savannahs and woodlands: the potential of multitemporal polarimetric RADARSAT-2 fine beam images. Remote Sens. Environ. 138, 215–231. http://dx.doi.org/10.1016/j.rse.2013.07.011.
Mayaux, P., Bartholomé, E., Fritz, S., Belward, A., 2004. A new land-cover map of Africa for the year 2000. J. Biogeogr. 31, 861–877. http://dx.doi.org/10.1111/j.1365-2699.2004.01073.x.
Mermoz, S., Le Toan, T., Villard, L., Réjou-Méchain, M., Seifert-Granzin, J., 2014. Biomass assessment in the Cameroon savanna using ALOS PALSAR data. Remote Sens. Environ. 155, 109–119. http://dx.doi.org/10.1016/j.rse.2014.01.029.
Mermoz, S., Réjou-Méchain, M., Villard, L., Le Toan, T., Rossi, V., Gourlet-Fleury, S., 2015. Decrease of L-band SAR backscatter with biomass of dense forests. Remote Sens. Environ. 159, 307–317. http://dx.doi.org/10.1016/j.rse.2014.12.019.
Michelakis, D., Stuart, N., Lopez, G., Linares, V., Woodhouse, I.H., 2014. Local-scale mapping of biomass in tropical lowland pine savannas using ALOS PALSAR. Forests 5, 2377–2399. http://dx.doi.org/10.3390/f5092377.
Mitchard, E.T.A., Flintrop, C.M., 2013. Woody encroachment and forest degradation in sub-Saharan Africa's woodlands and savannas 1982–2006. Philos. Trans. R. Soc. Lond. Ser. B Biol. Sci. 368. http://dx.doi.org/10.1098/rstb.2012.0406.
Mitchard, E.T.A., Saatchi, S.S., Woodhouse, I.H., Nangendo, G., Ribeiro, N.S., Williams, M., Ryan, C.M., Lewis, S.L., Feldpausch, T.R., Meir, P., 2009. Using satellite radar backscatter to predict above-ground woody biomass: a consistent relationship across four different African landscapes. Geophys. Res. Lett. 36, L23401. http://dx.doi.org/10.1029/2009GL040692.
Mitchard, E.T.A., Saatchi, S.S., Lewis, S.L., Feldpausch, T.R., Woodhouse, I.H., Sonké, B., Rowland, C., Meir, P., 2011. Measuring biomass changes due to woody encroachment and deforestation/degradation in a forest–savanna boundary region of central Africa using multi-temporal L-band radar backscatter. In: Remote Sensing of Environment, DESDynI VEG-3D Special Issue. 115. pp. 2861–2873. http://dx.doi.org/10.1016/j.rse.2010.02.022.
Mitchard, E.T.A., Saatchi, S.S., Baccini, A., Asner, G.P., Goetz, S.J., Harris, N.L., Brown, S., 2013a. Uncertainty in the spatial distribution of tropical forest biomass: a comparison of pan-tropical maps. Carbon Balance Manag. 8, 10. http://dx.doi.org/10.1186/1750-0680-8-10.
Mitchard, E.T.A., Meir, P., Ryan, C.M., Woollen, E.S., Williams, M., Goodman, L.E., Mucavele, J.A., Watts, P., Woodhouse, I.H., Saatchi, S.S., 2013b. A novel application of satellite radar data: measuring carbon sequestration and detecting degradation in a community forestry project in Mozambique. Plant Ecolog. Divers. 6, 159–170. http://dx.doi.org/10.1080/17550874.2012.695814.
Naidoo, L., Mathieu, R., Main, R., Kleynhans, W., Wessels, K., Asner, G., Leblon, B., 2015. Savannah woody structure modelling and mapping using multi-frequency (X-, C- and L-band) synthetic aperture radar data. ISPRS J. Photogramm. Remote Sens. 105, 234–250. http://dx.doi.org/10.1016/j.isprsjprs.2015.04.007.
Naidoo, L., Mathieu, R., Main, R., Wessels, K., Asner, G.P., 2016. L-band synthetic aperture radar imagery performs better than optical datasets at retrieving woody fractional cover in deciduous, dry savannahs. Int. J. Appl. Earth Obs. Geoinf. 52, 54–64. http://dx.doi.org/10.1016/j.jag.2016.05.006.
Notarnicola, C., Posa, F., 2004. Bayesian algorithm for the estimation of the dielectric constant from active and passive remotely sensed data. IEEE Geosci. Remote Sens. Lett. 1, 179–183. http://dx.doi.org/10.1109/LGRS.2004.827461.
O'Connor, T.G., Puttick, J.R., Hoffman, M.T., 2014. Bush encroachment in southern Africa: changes and causes. Afr. J. Range Forage Sci. 31, 67–88. http://dx.doi.org/10.2989/10220119.2014.939996.
Quegan, S., Yu, J.J., 2001. Filtering of multichannel SAR images. IEEE Trans. Geosci. Remote Sens. 39, 2373–2379. http://dx.doi.org/10.1109/36.964973.
Ramankutty, N., Gibbs, H.K., Achard, F., Defries, R., Foley, J.A., Houghton, R.A., 2007. Challenges to estimating carbon emissions from tropical deforestation. Glob. Chang. Biol. 13, 51–66. http://dx.doi.org/10.1111/j.1365-2486.2006.01272.x.
Réjou-Méchain, M., Muller-Landau, H.C., Detto, M., Thomas, S.C., Le Toan, T., Saatchi, S.S., Barreto-Silva, J.S., Bourg, N.A., Bunyavejchewin, S., Butt, N., Brockelman, W.Y., Cao, M., Cárdenas, D., Chiang, J.-M., Chuyong, G.B., Clay, K., Condit, R., Dattaraja, H.S., Davies, S.J., Duque, A., Esufali, S., Ewango, C., Fernando, R.H.S., Fletcher, C.D., Gunatilleke, I.A.U.N., Hao, Z., Harms, K.E., Hart, T.B., Hérault, B., Howe, R.W., Hubbell, S.P., Johnson, D.J., Kenfack, D., Larson, A.J., Lin, L., Lin, Y., Lutz, J.A., Makana, J.-R., Malhi, Y., Marthews, T.R., McEwan, R.W., McMahon, S.M., McShea, W.J., Muscarella, R., Nathalang, A., Noor, N.S.M., Nytch, C.J., Oliveira, A.A., Phillips, R.P., Pongpattananurak, N., Punchi-Manage, R., Salim, R., Schurman, J., Sukumar, R., Suresh, H.S., Suwanvecho, U., Thomas, D.W., Thompson, J., Uríarte, M., Valencia, R., Vicentini, A., Wolf, A.T., Yap, S., Yuan, Z., Zartman, C.E., Zimmerman, J.K., Chave, J., 2014. Local spatial structure of forest biomass and its consequences for remote sensing of carbon stocks. Biogeosciences 11, 6827–6840. http://dx.doi.org/10.5194/bg-11-6827-2014.
Ribeiro, N.S., Saatchi, S.S., Shugart, H.H., Washington-Allen, R.A., 2008. Aboveground biomass and leaf area index (LAI) mapping for Niassa Reserve, northern Mozambique. J. Geophys. Res. 113 G02S02. https://doi.org/10.1029/2007JG000550.
Saatchi, S.S., Harris, N.L., Brown, S., Lefsky, M., Mitchard, E.T.A., Salas, W., Zutta, B.R., Buermann, W., Lewis, S.L., Hagen, S., Petrova, S., White, L., Silman, M., Morel, A., 2011. Benchmark map of forest carbon stocks in tropical regions across three continents. PNAS 108, 9899–9904. http://dx.doi.org/10.1073/pnas.1019576108.
Sankaran, M., Hanan, N.P., Scholes, R.J., Ratnam, J., Augustine, D.J., Cade, B.S., Gignoux, J., Higgins, S.I., Le Roux, X., Ludwig, F., Ardo, J., Banyikwa, F., Bronn, A., Bucini, G., Caylor, K.K., Coughenour, M.B., Diouf, A., Ekaya, W., Feral, C.J., February, E.C., Frost, P.G.H., Hiernaux, P., Hrabar, H., Metzger, K.L., Prins, H.H.T., Ringrose, S., Sea, W., Tews, J., Worden, J., Zambatis, N., 2005. Determinants of woody cover in African savannas. Nature 438, 846–849. http://dx.doi.org/10.1038/nature04070.
Santoro, M., Askne, J., Smith, G., Fransson, J.E.S., 2002. Stem volume retrieval in boreal forests from ERS-1/2 interferometry. Remote Sens. Environ. 81, 19–35. http://dx.doi.org/10.1016/S0034-4257(01)00329-7.
Santoro, M., Beer, C., Cartus, O., Schmullius, C., Shvidenko, A., McCallum, I., Wegmüller, U., Wiesmann, A., 2011. Retrieval of growing stock volume in boreal forest using hyper-temporal series of Envisat ASAR ScanSAR backscatter measurements. Remote Sens. Environ. 115, 490–507. http://dx.doi.org/10.1016/j.rse.2010.09.018.
Santoro, M., Cartus, O., Fransson, J.E.S., Shvidenko, A., McCallum, I., Hall, R.J., Beaudoin, A., Beer, C., Schmullius, C., 2013. Estimates of forest growing stock volume for Sweden, Central Siberia, and Québec using Envisat advanced synthetic aperture radar backscatter data. Remote Sens. 5, 4503–4532. http://dx.doi.org/10.3390/rs5094503.
Saugier, B., Roy, J., Mooney, H.A., 2001. 23 - estimations of global terrestrial productivity: converging toward a single number? In: Terrestrial Global Productivity, Physiological Ecology. Academic Press, San Diego, pp. 543–557.
Sexton, J.O., Song, X.-P., Feng, M., Noojipady, P., Anand, A., Huang, C., Kim, D.-H., Collins, K.M., Channan, S., DiMiceli, C., Townshend, J.R., 2013. Global, 30-m resolution continuous fields of tree cover: Landsat-based rescaling of MODIS vegetation continuous fields with lidar-based estimates of error. Int. J. Digital Earth 6, 427–448. http://dx.doi.org/10.1080/17538947.2013.786146.
Shimada, M., Ohtaki, T., 2010. Generating large-scale high-quality SAR mosaic datasets: application to PALSAR data for global monitoring. IEEE J. Sel. Top. Appl. Earth Observ. Rem. Sens. 3, 637–656. http://dx.doi.org/10.1109/JSTARS.2010.2077619.
Shimada, M., Isoguchi, O., Tadono, T., Isono, K., 2009. PALSAR radiometric and geometric calibration. IEEE Trans. Geosci. Remote Sens. 47, 3915–3932. http://dx.doi.org/10.1109/TGRS.2009.2023909.
Shimada, M., Itoh, T., Motooka, T., Watanabe, M., Shiraishi, T., Thapa, R., Lucas, R., 2014. New global forest/non-forest maps from ALOS PALSAR data (2007–2010). Remote Sens. Environ. 155, 13–31. http://dx.doi.org/10.1016/j.rse.2014.04.014.
Staver, A.C., Archibald, S., Levin, S.A., 2011. The global extent and determinants of savanna and Forest as alternative biome states. Science 334, 230–232. http://dx.doi.org/10.1126/science.1210465.
Tarantola, A., 2005. Inverse Problem Theory and Methods for Model Parameter Estimation, Other Titles in Applied Mathematics. Society for Industrial and Applied Mathematics.
Urbazaev, M., Thiel, C., Mathieu, R., Naidoo, L., Levick, S.R., Smit, I.P.J., Asner, G.P., Schmullius, C., 2015. Assessment of the mapping of fractional woody cover in southern African savannas using multi-temporal and polarimetric ALOS PALSAR L-band images. Remote Sens. Environ. 166, 138–153. http://dx.doi.org/10.1016/j.rse.2015.06.013.
Valentini, R., Arneth, A., Bombelli, A., Castaldi, S., Cazzolla Gatti, R., Chevallier, F., Ciais, P., Grieco, E., Hartmann, J., Henry, M., Houghton, R.A., Jung, M., Kutsch, W.L., Malhi, Y., Mayorga, E., Merbold, L., Murray-Tortarolo, G., Papale, D., Peylin, P., Poulter, B., Raymond, P.A., Santini, M., Sitch, S., Vaglio Laurin, G., van der Werf, G.R., Williams, C.A., Scholes, R.J., 2014. A full greenhouse gases budget of Africa: synthesis, uncertainties, and vulnerabilities. Biogeosciences 11, 381–407. http://dx.doi.org/10.5194/bg-11-381-2014.
Villard, L., 2009. Forward & Inverse Modeling for Synthetic Aperture Radar Observables in Bistatic Configuration. In: Applications in Forest Remote Sensing (PhD thesis). Institut Supérieur de l'Aéronautique et de l'Espace.
Villard, L., Borderies, P., 2015. On the use of virtual ground scatterers to localize double and triple bounce scattering mechanisms for bistatic SAR. J. Electromagn. Waves Applic. 29, 626–635. http://dx.doi.org/10.1080/09205071.2015.1012594.
White, F., 1984. The Vegetation of Africa: A Descriptive Memoir to Accompany the Unesco/Aetfat/Unso Vegetation Map of Africa and Map. United Nations Educational, Paris.
Williams, C.A., Hanan, N.P., Neff, J.C., Scholes, R.J., Berry, J.A., Denning, A.S., Baker, D.F., 2007. Africa and the global carbon cycle. Carbon Balance Manag. 2, 3. http://dx.doi.org/10.1186/1750-0680-2-3.
Yu, Y., Saatchi, S., 2016. Sensitivity of L-band SAR backscatter to aboveground biomass of global forests. Remote Sens. 8, 522. http://dx.doi.org/10.3390/rs8060522.
Zeidler, J., Wegmann, M., Dech, S., 2012. In: Michel, U., Civco, D.L., Ehlers, M., Schulz, K., Nikolakopoulos, K.G., Habib, S., Messinger, D., Maltese, A. (Eds.), Spatio-temporal Robustness of Fractional Cover Upscaling: A Case Study in Semi-arid Savannah's of Namibia and Western Zambia, pp. 85380S. http://dx.doi.org/10.1117/12.970623.